European Cells and Materials Vol.57 2026 (pages 121–141) DOI: 10.22203/eCM.v057a06 ISSN 1473-2262

Original Article

ACTIVATION OF PIEZO1 BY PFP@R-LIP COMBINED WITH LOW-INTENSITY PULSED ULTRASOUND SUPPRESSES HEPATOCELLULAR CARCINOMA PROGRESSION AND IMPROVES ANTITUMOR IMMUNITY

Jian Jiang[1], Xinling Du[1], Weidong Wang[1], Mingming Li[1], Yingxuan Mao[1], Mingwei Zhu[1], Linlin Han[1], Jiamei Niu[1] and Xiuhua Yang[1,*]

[1]Department of Ultrasound, The First Affiliated Hospital of Harbin Medical University, 150001 Harbin, Heilongjiang, China

Abstract

Background: Insufficient drug targeting and the immunosuppressive tumor microenvironment are key factors contributing to the high mortality rate of hepatocellular carcinoma (HCC). The targeted cavitation effect mediated by low-intensity pulsed ultrasound (LIPUS) provides a promising strategy to address these challenges. Although Piezo1 is known to be dysregulated in multiple cancer types, it remains unclear whether ultrasound stimulation can activate Piezo1 and trigger downstream cell death and immune activation. **Methods:** Perfluoropentane (PFP)@R-Lip was prepared to assess its combined effects with LIPUS on proliferation, migration, invasion, apoptosis, and ferroptosis in HCC cells. The specific Piezo1 inhibitor GsMTx4 was used to verify the role of Piezo1 activation and immunogenic cell death (ICD) induction. A tumor-bearing mouse model was established to validate the *in vivo* antitumor efficacy of LIPUS combined with PFP@R-Lip. Student's t-test, one-way ANOVA test, and two-way ANOVA test were used. **Results:** PFP@R-Lip was successfully prepared and exhibited enhanced targeting ability to HCC cells. The combination of LIPUS and PFP@R-Lip inhibited the proliferation, migration, invasion, and cell cycle of HCC cells. Mechanistically, the combination activated the Piezo1 channel, leading to intracellular calcium overload, mitochondrial membrane potential (MMP) depolarization, and reactive oxygen species (ROS) accumulation. This cascade induced both apoptosis and ferroptosis, ultimately triggering ICD. These effects were partially reversed by pretreatment with GsMTx4. **Conclusions:** PFP@R-Lip with ultrasound imaging properties and tumor-targeting specificity was developed. LIPUS combined with PFP@R-Lip was verified to induce intracellular calcium overload and synergistically trigger apoptosis and ferroptosis to prompt ICD in HCC via Piezo1 activation.

Keywords: Low-intensity pulsed ultrasound, hepatocellular carcinoma, targeted phase-change liposomes, Piezo1, immunogenic cell death.

***Address for correspondence**: Xiuhua Yang, Department of Ultrasound, The First Affiliated Hospital of Harbin Medical University, 150001 Harbin, Heilongjiang, China. E-mail: yangxiuhua@hrbmu.edu.cn.

Introduction

Hepatocellular carcinoma (HCC) represents a major global health burden, currently ranking as the sixth most diagnosed cancer and the third leading cause of cancer-related mortality worldwide [1]. Immunogenic cell death (ICD) has emerged as a promising therapeutic strategy, aiming to convert tumor cells into an endogenous vaccine to stimulate systemic antitumor immunity [2]. However, the clinical translation of ICD-based approaches for HCC is hindered by several critical challenges. The inherently immunosuppressive tumor microenvironment of HCC, characterized by M2-polarized tumor-associated macrophages (TAMs) and an abundance of regulatory T cells, actively impairs effective immune responses [3]. Moreover, conventional therapies that mainly induce apoptosis often elicit ICD of limited potency due to the intrinsically low immunogenicity of apoptotic cell death [4]. Additionally, the lack of tumor-targeting specificity in current modalities leads to off-target effects and immune-related adverse events, further reducing therapeutic efficacy [5]. Thus, developing novel strategies capable of precise tumor targeting and inducing highly immunogenic form of cell death has become a critical unmet need in clinical practice.

The rapid development of ultrasound offers a promising avenue to address these challenges. Low-intensity pulsed ultrasound (LIPUS) provides a non-invasive modal-

ity for delivering localized mechanical energy to tissues. Its therapeutic potential lies in its bioeffects, including cavitation and acoustic radiation force [6]. The integration of targeted, gas-core liposomes with LIPUS can not only improve treatment precision but also effectively reduce the cavitation threshold, thus minimizing potential injury to adjacent normal tissues [7]. Despite this potential, the mechanisms by which LIPUS-mediated mechanical force induces HCC cell death remain insufficiently explored. Piezo1, a mechanosensitive ion channel, is a key molecular transducer that converts external mechanical stimuli into intracellular electrochemical signals via calcium influx [8]. Studies have shown that Piezo1 is frequently overexpressed in multiple malignancies and is closely associated with tumor immunosuppression and metastatic potential [9]. Ultrasound-induced membrane deformation via cavitation and radiation force is a potent activator of Piezo1 channels [10–12]. However, the specific role and mechanistic contribution of ultrasound-induced Piezo1 activation in HCC progression remain largely unclear, hindering the translation of mechanobiological insights into novel HCC therapies.

Calcium influx mediated by Piezo1 activation has been reported to induce ferroptosis, which is characterized by the impairment of glutathione-dependent antioxidant defenses and membrane rupture [13,14]. Importantly, ferroptosis is accompanied by the massive release of damage-associated molecular patterns (DAMPs), conferring strong immunogenic potential and making it an attractive target for ICD [15]. A major challenge for the clinical application of ferroptosis-based therapy is the lack of tumor-selective inducers, which often cause systemic toxicity. The spatially focused energy delivery of LIPUS combined with the tumor-targeting ability of functionalized liposomes, may provide a solution to achieve localized ferroptosis induction.

Herein, c-RGD-modified liposomes encapsulating perfluoropentane (PFP), abbreviated as PFP@R-Lip, were prepared to actively target integrins overexpressed on HCC cells via the c-RGD moiety. Under LIPUS irradiation, the PFP core undergoes a liquid-to-gas phase transition, enabling ultrasound imaging. Meanwhile, the PFP gas core can further amplify the localized mechanical effects of LIPUS, thereby activating Piezo1 channels on HCC cells. The subsequent Piezo1-mediated intracellular calcium overload is expected to trigger apoptosis and ferroptosis, which can overcome the low immunogenicity of apoptosis to a certain extent. The study aims to establish a theoretical foundation for developing a precise, mechanobiology-based therapeutic strategy for HCC treatment.

Materials and Methods

Cells and Reagents

HCCLM3, Hepa 1-6, and WRL68 cells were purchased from the Institute of the Chinese Academy of Sciences. Distearoyl-sn-glycero-3-phosphocholine (DSPC), 1,2-distearoyl-sn-glycero-3-phosphoethanolamine-N-[methoxy (polyethylene glycol)-2000] (DSPE-mPEG2000), DSPE-mPEG2000-cRGD and cholesterol were obtained from Xi'an Ruixi Biotechnology Co., Ltd. PFP was purchased from MedChemExpress LLC. DiI (1,1′-dioctadecyl-3,3,3′,3′-tetramethylindocarbocyanine perchlorate) was obtained from Beyotime Biotechnology Inc.

Preparation of Liposome

Liposomes were prepared via the thin-film hydration and ultrasonic emulsification method. Briefly, 2 mg cholesterol, 2 mg DSPE-mPEG2000, and 6 mg DSPC were dissolved in 4 mL dichloromethane. The mixture was evaporated at 50 °C to form a lipid film. Then, 3 mL PBS was added for hydration, followed by the addition of 100 μL PFP. The mixture was subjected to ultrasonic emulsification to form the non-targeted PFP@Lip, which were then purified by centrifugation and sterilized by membrane filtration. For the preparation of targeted PFP@R-Lip, DSPE-mPEG2000 was replaced with DSPE-mPEG2000-cRGD, and all other procedures were the same as those for PFP@Lip. For the synthesis of PFP/DiI@R-Lip and PFP/DiI@Lip, 0.1 mg DiI was mixed with the lipid materials and co-dissolved in dichloromethane, with the remaining steps consistent with those of PFP@R-Lip and PFP@Lip, respectively.

Liposome Characterization

An optical microscope (Olympus, Tokyo, Japan) and transmission electron microscopy (Hitachi, Tokyo, Japan) were used for morphological observation of PFP@R-Lip and PFP@Lip. The hydrated particle sizes and zeta potentials of PFP@R-Lip and PFP@Lip were determined using a dynamic light scattering instrument (Malvern Panalytical Ltd., Worcestershire, UK), and the particle size was measured on the 1st, 3rd, 5th, and 7th days after preparation.

Phase Transition and Ultrasonic Imaging of PFP@R-Lip

The phase transition of PFP from liquid to gas was indirectly verified by observing the particle size changes of PFP@R-Lip after LIPUS using an optical microscope. For ultrasonic imaging, PFP@R-Lip was added into the prefabricated pores of the agarose phantom, followed by LIPUS exposure at different acoustic intensities (Con, 0.5 W/cm^2, 1 W/cm^2, 2 W/cm^2, 3 W/cm^2) for 1 min or 2 min. The gray and contrast values were detected by the Aplio i900 diagnostic ultrasound system (Canon, Tokyo, Japan).

Cellular Uptake of PFP/DiI@R-Lip and PFP/DiI@Lip

To verify the cellular uptake of PFP@R-Lip and PFP@Lip, DiI was incorporated into the liposomal membrane for the preparation of PFP/DiI@R-Lip and PFP/DiI@Lip. HCCLM3 cells were co-cultured with 20

μg/mL PFP/DiI@R-Lip or PFP/DiI@Lip for 1 h, 3 h, and 9 h, respectively. And the cells were subjected to flow cytometric analysis (BD Biosciences, CA, US) or observed by a laser scanning confocal microscope (Carl Zeiss AG, Oberkochen, Germany).

Finite Element Simulation of Acoustic Field Distribution

The Acoustics Module integrated in COMSOL Multiphysics software (version 6.4, COMSOL AB, Stockholm, Sweden) was employed for the simulation. The parameters of the ultrasonic transducer were set as follows: diameter of 3 cm, focal length of 1.5 cm, frequency of 1 MHz, acoustic intensity of 2 W/cm^2, and duty cycle of 50%. The medium parameters were configured with a density of 1000 kg/m^3 and a sound velocity of 1540 m/s. A full three-dimensional model was established via the pressure acoustics, frequency domain physics interface, followed by visualization of the simulated acoustic field distribution.

Experimental Animals, LIPUS Parameters, and Liposome Dosages

C57BL/6 mice (6–8 weeks old) were provided by Jiangsu Huachuang Xinnuo Pharmaceutical Technology Co., Ltd. and housed under specific pathogen-free conditions. The animal experimental protocol was approved by the Animal Ethics Committee of the First Affiliated Hospital of Harbin Medical University (Approval No. 2024052). The LIPUS transducer was characterized by a frequency of approximately 1 MHz, a focal length of 1.5 cm, and a diameter of 3 cm, with a duty cycle of 50%. For *in vitro* experiments, cells were exposed to LIPUS for 1 min. Specifically, 20 μg/mL of PFP@R-Lip or PFP@Lip was added to the cell culture 9 h before LIPUS. For the subsequent experiments, the cells were divided into 8 groups (n = 5): G1 (control), G2 (pretreated with 5 μM GsMTx4 for 0.5 h), G3 (pretreated with 20 μg/mL PFP@R-Lip for 9 h, followed by 2 W/cm^2 LIPUS for 1 min), G4 (pretreated with 20 μg/mL PFP@R-Lip for 9 h and 5 μM GsMTx4 for 0.5 h, followed by 2 W/cm^2 for 1 min), G5 (knockdown of Piezo1 by siRNA), G6 (knockdown of Piezo1 by siRNA, pretreated with 20 μg/mL PFP@R-Lip for 9 h, followed by 2 W/cm^2 LIPUS for 1 min), G7 (pretreated with 1 μM Ferrostatin-1 for 1 h) and G8 (pretreated with 20 μg/mL PFP@R-Lip for 9 h and 1 μM Ferrostatin-1 for 1 h, followed by 2 W/cm^2 for 1 min). For the *in vivo* experiments, C57BL/6 mice were divided into four groups: mG1 (control), mG2 (intraperitoneal injection of 1 mg/kg GsMTx4), mG3 (pretreated with 200 μL of 2 mg/mL PFP@R-Lip via tail vein injection for 9 h, followed by 2 W/cm^2 LIPUS for 2 min), and mG4 (pretreated with 200 μL of 2 mg/mL PFP@R-Lip via tail vein injection for 9 h and 1 mg/kg GsMTx4 via intraperitoneal injection for 0.5 h, followed by 2 W/cm^2 LIPUS for 2 min). The intervention was administered every other day for a total of three sessions.

MTT Assay

HCCLM3 cells were seeded in 96-well plates, and 20 μg/mL of PFP@R-Lip was added to the cells. After 9 h of incubation, the cells were exposed to LIPUS with different acoustic intensities, followed by further incubation for 24–48 h. Then the cells were assayed in accordance with the MTT assay protocol.

Calcein-AM/PI Staining

HCCLM3 cells were seeded in confocal dishes, and 20 μg/mL of PFP@R-Lip was added for another 9 h of incubation. The cells were then irradiated with LIPUS of different acoustic intensities for 1 min, followed by 24 h incubation. After rinsing with PBS, 1 mL Calcein-AM/PI working solution was added to each confocal dish for 15 min. Finally, the cells were observed under a laser scanning confocal microscope.

Colony Formation Assay

HCCLM3 cells were seeded in 6-well plates at a density of approximately 1000 cells per well, and 20 μg/mL of PFP@R-Lip was added for further incubation for 9 h. The cells were subsequently irradiated with LIPUS of different acoustic intensities for 1 min, and the culture was maintained for 14 days with medium refreshed every 3 days. Then, the cells were fixed and stained.

Tumor Sphere Inhibition

Matrigel was added to a 96-well plate and incubated for 2 h to allow gelation, to form a low-adhesion microenvironment. Then, approximately 10^5 cells were seeded into each well and continuously cultured for 7 days until the tumor spheres reached a diameter of approximately 100 μm. Thereafter, 20 μg/mL PFP@R-Lip was added to the wells for another 9 h of incubation, followed by LIPUS irradiation with different acoustic intensities for 1 min. The tumor spheres were further cultured for 3 days, then photographed and analyzed.

Transwell Assay

For migration, cells were resuspended in FBS-free medium and seeded into the upper chambers of transwell inserts. 500 μL medium containing 10% FBS was added to the lower chambers. After cell adherence, 20 μg/mL of PFP@R-Lip was added to the upper chambers for 1 h incubation, followed by 1 min LIPUS irradiation. After 24 h of incubation, the cells on the lower side of the membrane were fixed and stained. For cell invasion, the upper chambers were pre-coated with Matrigel before cell seeding, and the subsequent procedures were repeated in accordance with the cell migration assay.

Flow Cytometry Assay for Apoptosis and Cell Cycle

Cells treated with different intervention regimens were collected, rinsed, and then resuspended to a density

of approximately 1×10^6/ mL. 100 μL cell suspension was transferred into flow cytometry tubes, followed by the addition of staining solution in accordance with the apoptosis or cell cycle manufacturer's protocol (Cat. No. C1062S, Beyotime, Shanghai, China). After incubation in the dark, the cells were subjected to flow cytometric analysis.

Detection of Intracellular Calcium

Cells were washed three times with PBS, followed by incubation with 2 μM Fluo-4 AM (Cat. No. S1060, Beyotime, Shanghai, China) at 37 °C for 20 min in the dark to complete fluorescent probe loading. After incubation, the supernatant was discarded, and cells were rinsed three times with PBS to remove extracellular probes. Subsequently, cells were treated with different interventions according to experimental grouping. The intracellular calcium fluorescence intensity was observed and imaged using a laser scanning confocal microscope immediately.

Detection of Intracellular Reactive Oxygen Species (ROS)

After being treated with different interventions according to experimental grouping, cells were incubated for another 24 h. DCFH-DA (Cat. No. S0033S, Beyotime, Shanghai, China) was diluted to prepare a working solution with a concentration of 10 μM. After the culture medium was discarded, 1 mL DCFH-DA working solution was added to the cells. The cells were incubated at 37 °C for 20 min in the dark. Thereafter, the cells were washed three times with PBS to eliminate extracellular DCFH-DA. Fluorescence signals were detected and observed using a laser scanning confocal microscope.

Detection of Mitochondrial Membrane Potential (MMP)

After being treated with different interventions according to experimental grouping, cells were incubated for another 24 h. Then, cells were washed with PBS and incubated with JC-1 (Cat. No. C2003S, Beyotime, Shanghai, China) working solution (10 μM) at 37 °C in a cell incubator for 20 min. After incubation, the supernatant was discarded, and the cells were rinsed three times with PBS. Finally, Fluorescence signals were detected and observed using a laser scanning confocal microscope.

Detection of Intracellular Ferrous Ion

After being treated with different interventions according to experimental grouping, cells were incubated for another 24 h. After removing the medium, cells were washed with PBS, and then incubated with the RhoNox-6 (Cat. No. S1070S, Beyotime, Shanghai, China) working solution (2 μM) at 37 °C in the dark for 30 min. Subsequently, cells were rinsed three times with PBS. The fluorescence signals were visualized and imaged using a laser scanning confocal microscope.

Detection of Lipid Peroxidation

After being treated with different interventions according to experimental grouping, cells were incubated for another 24 h. The C11-Bodipy (Cat. No. SML3717, Sigma-Aldrich, St. Louis, USA) was diluted to a final concentration of 2 μM with serum-free medium. After removing the medium, cells were washed with PBS, and then incubated with the C11-Bodipy (2 μM) at 37 °C in the dark for 30 min. Subsequently, cells were rinsed three times with PBS. The fluorescence signals were visualized and imaged using a laser scanning confocal microscope.

Database

RNA data of Piezo1 and survival analysis were obtained from the open database (TCGA) at http://gepia2.cancer-pku.cn and https://ualcan.path.uab.edu.

Transcriptomics Sequencing

HCCLM3 cells were treated with LIPUS + PFP@R-Lip (pretreated with 20 μg/mL PFP@R-Lip for 9 h, followed by 2 W/cm^2 LIPUS for 1 min), and the control group was left untreated. After culturing for 24 h, cells were collected. Total RNA was extracted using the TRIzol reagent according to the protocol. The libraries were sequenced on an Illumina Novaseq 6000 platform, and 150 bp paired-end reads were generated. Q value < 0.05 and foldchange > 2 or foldchange < 0.5 were set as the threshold for significantly differential expression gene. The transcriptome sequencing and analysis were conducted by OE Biotech Co., Ltd. (Shanghai, China).

Western Blotting

Procedures were the same as previously published article [16]. Briefly, proteins were extracted, electrophoresed, and transferred to polyvinylidene fluoride membranes. Then the membranes were blocked with 5% milk and incubated with antibodies. All the antibodies, including E-cadherin (Cat. No. 20874-1-AP), N-cadherin (Cat. No. 22018-1-AP), Vimentin (Cat. No. 10366-1-AP), GPX4 (Cat. No. 30388-1-AP), xCT (Cat. No. 32384-1-AP), ACSL4 (Cat. No. 22401-1-AP), Piezo1 (Cat. No. 15939-1-AP), Bax (Cat. No. 50599-2-Ig), Bcl-2 (Cat. No. 12789-1-AP), cleaved Caspase-3 (Cat. No. 19677-1-AP), β-actin (Cat. No. 66009-1-Ig) were supplied by Proteintech Co., Ltd (Wuhan, China). Protein bands were visualized with an enhanced chemiluminescence reagent (Cat. No. P0018S, Beyotime, Shanghai, China).

Immunofluorescence

Cells were cultured on glass coverslips, followed by different treatments. After 24 h, the cells were fixed with 4% paraformaldehyde, permeabilized by 0.25% TritonX-100 and blocked with 1% BSA. Then the cells were incubated with primary antibodies and a secondary antibody. Finally, DAPI was added to stain the nuclei. The images

were captured by a laser confocal microscope.

Small-interfering RNA (siRNA) Transfection

Cell transfection was performed using Lipofectamine 2000® (Cat. No. 11668019, Thermo Fisher Scientific, Inc.). siRNA was designed by Sangon Biotech (Shanghai) Co., Ltd. For each well of a six-well plate, 3 μL siRNA (sequences in **Supplementary Table 1**) and 5 μL Lipofectamine 2000® were separately diluted in 250 μL Opti-MEM Reduced Serum Medium. Final siRNA concentration was 100 nM. After a 5-min incubation at room temperature, the two solutions were combined, and then added to cells previously rinsed with serum-free medium. Following 6 h of incubation at 37 °C, the transfection mixture was replaced with complete culture medium. The following experiments were started after 24 h.

Detection of HMGB1 and ATP

HCCLM3 cells were subjected to interventions according to the four groups: G1, G2, G3, and G4. After 24 h, the supernatant was collected. An ELISA kit (Cat. No. JL13693, Jianglai Biotech, Shanghai, China) was used to detect HMGB1. Briefly, the standard solution and supernatant were added to the wells and incubated for 60 min. After discarding the liquid, the biotinylated antibody was introduced, followed by 60 min incubation. Subsequently, the HRP conjugate working solution, TMB substrate, and stop solution were added sequentially, and the absorbance of each well was measured immediately at 450 nm. An ATP assay kit (Cat. No. S0026, Beyotime, Shanghai, China) was used to detect ATP. Briefly, the working solution was added to each well and incubated for 5 min. Then sequentially add the standard solution and supernatant for 10 min of incubation. The ATP content was measured using a microplate reader.

In Vivo Antitumor Effect

First, 2×10^6 Hepa 1-6 cells were injected into the right back of every C57BL/6 mouse to establish a subcutaneous tumor model. When the tumor volume reached approximately 100 mm^3, the mice were randomly divided into 4 groups (aforementioned): G1, G2, G3, and G4. Interventions were performed every other day for a total of three sessions. Body weight was recorded every three days. Tumor volume was measured on the 7th, 14th, and 21st days. Tumor volume was calculated using the formula: Volume = L (longest diameter)$\times$ W^2 (shortest diameter) / 2. After 21 days, the tumor tissues were dissected and weighed. Tumors and major organs were prepared for H&E staining, TUNEL assay, and immunohistochemical detection of Ki67, GPX4, ACSL4, and xCT.

Tumor Targeting Evaluation

Tumor-bearing C57BL/6 mice were intravenously injected with 200 μL of PFP/DiI@R-Lip or PFP/DiI@Lip at a concentration of 2 mg/mL via the tail vein. At 9 h post-injection, the mice were euthanized, and the heart, liver, spleen, lungs, kidneys, and tumors were dissected. Fluorescence images were acquired using an *in vivo* imaging system (PerkinElmer, MA, USA)

In Vivo Antitumor Immunity

The DCs' maturation within tumors and spleens of C57BL/6 mice was analyzed by flow cytometry. Single-cell suspensions were prepared from dissected spleens and tumors of mice in each group. The cells were incubated with appropriately fluorescence-labeled antibodies (FITC-CD11c (Cat. No. E-AB-F0991C), APC-CD80 (Cat. No. E-AB-F0992E), PE-CD86 (Cat. No. E-AB-F0994D)) at 4 °C in the dark for 30 min before being subjected to flow cytometric analysis. Similarly, the polarization of TAMs in tumor tissue was assessed via flow cytometry. Tumor tissues were digested into single-cell suspensions and stained with fluorescence labeled antibodies (FITC-F4/80 (Cat. No. E-AB-F0995C), PE-CD86 (Cat. No. E-AB-F0994D), and APC-CD206 (Cat. No. E-AB-F1135E)) under dark conditions for 30 min before analysis. All fluorochrome-conjugated antibodies were purchased from Elabscience Biotechnology Co., Ltd. Additionally, the TNF-α (Cat. No. JL10484) and IL-6 (Cat. No. JL14113) levels in serum were quantified using commercial ELISA kits (Jianglai Biotech, Shanghai, China) according to the manufacturer's protocols.

Statistical Analysis

All data are presented as mean $\pm$ SEM. All *in vitro* experiments were repeated three times independently, and n = 5 mice per group for *in vivo* experiments. Group comparisons were analyzed using a Student's t-test, one-way ANOVA test, or two-way ANOVA test, and multiple comparisons were adjusted using the Tukey method using GraphPad Prism 7.0 (GraphPad Software, Inc., San Diego, CA, USA). Difference was considered to be significant when $p < 0.05$, $p < 0.01$ and $p < 0.001$.

Results

Characterization of PFP@Lip and PFP@R-Lip

PFP@Lip and PFP@R-Lip appeared as uniformly dispersed spherical vesicles with no obvious morphological differences between them under optical microscopy and transmission electron microscopy (Fig. 1**A** and **Supplementary Fig. 1**). Dynamic light scattering measurements indicated the hydrodynamic diameter of PFP@Lip was 237.8 $\pm$ 74.4 nm, and PFP@R-Lip was 243.1 $\pm$ 79.3 nm (Fig. 1**B** and **Supplementary Fig. 2**). Zeta potential analysis showed that the surface potential of PFP@Lip was –26.6 $\pm$ 4.5 mV and PFP@R-Lip was –16.6 $\pm$ 4.1 mV (Fig. 1**C**). To evaluate the stability of PFP@R-Lip, its hydrodynamic diameter was monitored continuously on days 1, 3, 5, and 7 at 4 °C. The results confirmed that there was no

significant difference in hydrodynamic size across the different time points (**Supplementary Fig. 3**).

Acoustic Field Distribution of LIPUS and Ultrasonic Imaging of PFP@R-Lip

Fig. 1**E** showed the acoustic pressure distribution on the transverse plane (XY plane) at a distance of 15 mm from the probe. When the acoustic intensity was set as 2 W/cm^2, the acoustic field exhibited a distinct circularly symmetric pattern, with a central low-pressure zone (blue, about -0.5 MPa) surrounded by alternating high-pressure rings and low-pressure rings. The acoustic pressure contours were concentric, indicating that the probe generated a typical axisymmetric annular focused field. And the acoustic field showed multiple discrete high-pressure and low-pressure zones alternating along the axial direction (Z-direction). A clear high-pressure focus was observed near Z = 15 mm, demonstrating that the probe achieved effective focusing. Following 2 min of irradiation with LIPUS at an intensity of 2 W/cm^2, the particle size of the PFP@R-Lip nanoparticles increased **(Supplementary Fig. 4**). This observation indirectly confirmed the liquid-to-gas phase transition of the PFP core induced by LIPUS. To further evaluate the ultrasound imaging performance of PFP@R-Lip, the nanoparticles were exposed to LIPUS at different acoustic intensities for 1 or 2 min, and were then examined using B-mode and contrast mode ultrasound imaging. Compared with the non-irradiated group (Con), the LIPUS-irradiated groups showed significantly enhanced ultrasound echo signals in both modes, confirming that the phase-transitioned PFP core can provide the nanoparticles with excellent ultrasound imaging capability. Within the acoustic intensity range of 0–2 W/cm^2, both B-mode and contrast mode imaging signals increased progressively with rising LIPUS intensity. Moreover, at the same acoustic intensity, the signal intensity was higher in the 2-min irradiation group than in the 1-min group. However, when the LIPUS intensity was increased to 3 W/cm^2 and the irradiation time extended to 2 min, the ultrasound signals in both imaging modes showed a noticeable decline (Fig. 1**D** and **Supplementary Fig. 5**). The observed decrease may be attributed to structural damage of PFP@R-Lip induced by excessive acoustic intensity and prolonged irradiation time.

Enhanced Uptake of PFP@R-Lip via c-RGD in HCCLM3 Cells

DiI-labeled PFP@Lip and PFP@R-Lip were constructed to evaluate the cellular uptake by HCCLM3 cells. Immunofluorescence results showed the red fluorescence (DiI) gradually increased with prolonged co-incubation time of HCCLM3 cells with DiI/PFP@R-Lip or DiI/PFP@Lip. Due to the targeting ability of the c-RGD peptide modified on the surface of PFP@R-Lip, the uptake of DiI/PFP@R-Lip by HCCLM3 cells was higher than that of DiI/PFP@Lip at each time point (Fig. 1**F**). Flow cytometry further confirmed that the intensity of intracellular DiI fluorescence increased progressively with longer co-incubation times. At all time points, the cellular uptake of the targeted DiI/PFP@R-Lip was significantly greater than that of the non-targeted DiI/PFP@Lip (Fig. 1**G**). Statistical analysis revealed that after 1 h, 3 h, and 9 h co-incubation, the uptake efficiency of DiI/PFP@R-Lip was approximately 1.5-fold, 1.2-fold, and 1.3-fold higher compared to the DiI/PFP@Lip group. Moreover, compared to the 1 h incubation group, the uptake of DiI/PFP@R-Lip increased by 2.7-fold after 9 h of incubation (Fig. 1**H**).

Inhibitory Effect of LIPUS Combined With PFP@R-Lip on HCCLM3 Cells

MTT assay showed that when HCCLM3 cells were treated with 0.5 W/cm^2 LIPUS combined with PFP@R-Lip, no significant difference in cell viability was observed between 24 h and 48 h. However, as the LIPUS intensity increased, cell survival showed a dose-dependent decline, and the number of viable cells continued to decrease from 24 h to 48 h. When the LIPUS intensity was raised to 2.5 W/cm^2, only a few viable cells remained (Fig. 2**A**). Consistent with the MTT assay, Calcein/PI staining revealed that the number of green-fluorescent viable cells did not decrease significantly after LIPUS treatment at 0.5 W/cm^2. As intensity further increased, the number of viable cells decreased gradually, while the number of red-fluorescent dead cells increased markedly (Fig. 2**B**). Colony formation assays demonstrated that the number of HCCLM3 cell colonies co-incubated with PFP@R-Lip decreased significantly with the increase in LIPUS intensity, and the colony size also tended to be reduced (Fig. 2**C**). The results of the tumor sphere assay exhibited a similar trend (**Supplementary Fig. 6**). Cell cycle analysis revealed an increase in the G2/M phase population after treatment with increasing intensities of LIPUS combined with PFP@R-Lip. (Fig. 2**D**). Statistical analysis indicated that the proportion of cells arrested at the G2/M phase increased to approximately 1.6-fold and 2.1-fold of that in the Con after treatment with LIPUS at 1 W/cm^2 and 2 W/cm^2 combined with PFP@R-Lip, respectively (Fig. 2**E**). LIPUS at 0–1 W/cm^2 combined with PFP@R-Lip (which exerted minimal effects on cell viability) was used to investigate the migration and invasion of HCCLM3 cells. Transwell assays showed that the number of cells that migrated and invaded into the lower chamber was significantly reduced at 24 h after LIPUS combined with PFP@R-Lip. The number of migrated cells in the 0.5 W/cm^2 and 1 W/cm^2 LIPUS groups was approximately 0.67-fold and 0.29-fold of that in the Con group, respectively. And the number of invasive cells in the 0.5 W/cm^2 and 1 W/cm^2 groups was about 0.53-fold and 0.24-fold of that in the Con group, respectively (Fig. 2**F**–**G**).

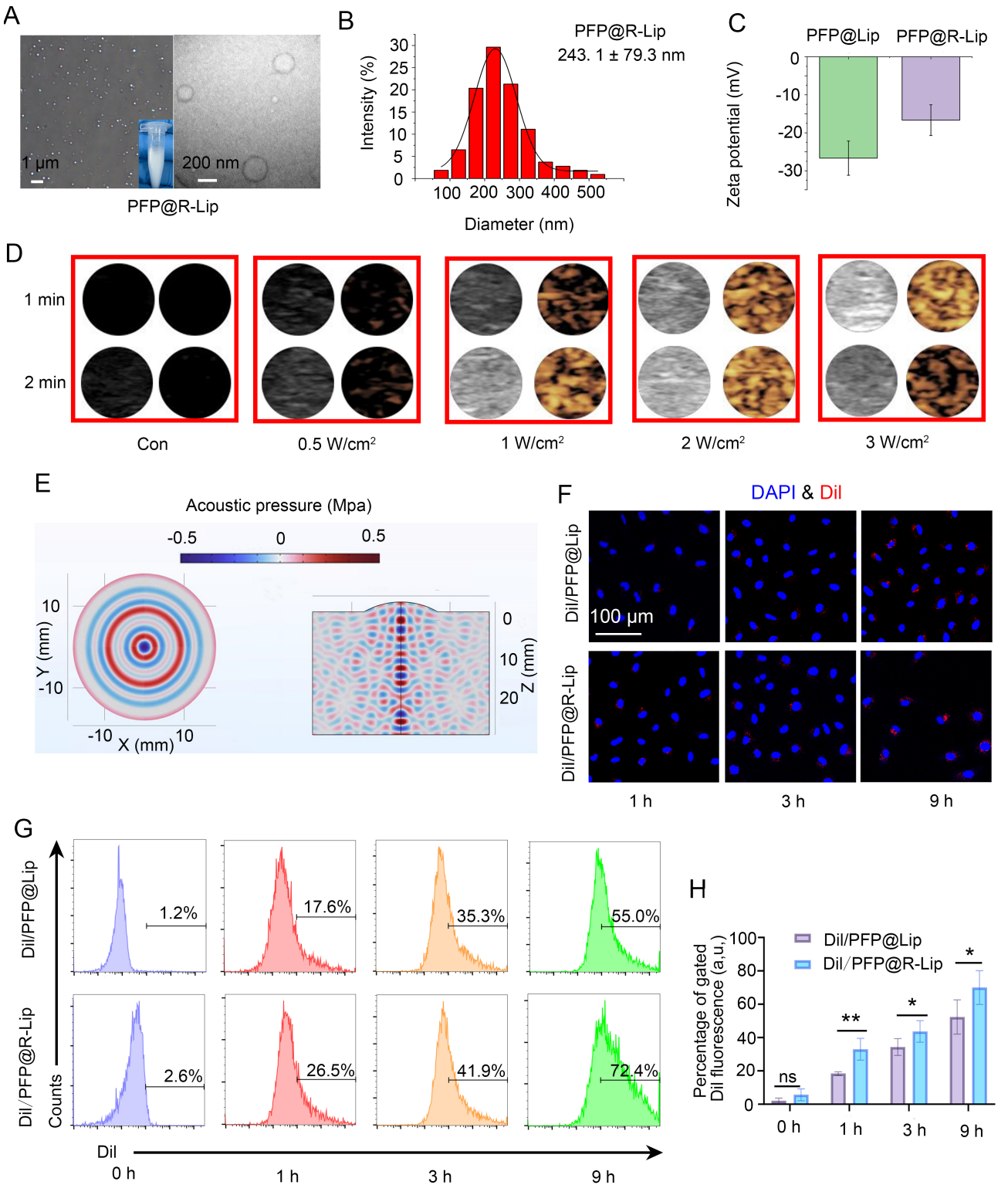

Fig. 1. Characterization of PFP@Lip & PFP@R-Lip and acoustic field simulation. (**A**) Morphological observations of PFP@R-Lip via Optical microscopy (left, scale bar = 1 μm) and transmission electron microscope (right, scale bar = 200 nm). (**B**) Hydrodynamic size of PFP@R-Lip. (**C**) Zeta Potential of PFP@Lip and PFP@R-Lip. (**D**) Ultrasound imaging (left: B-mode, right: contrast mode) of PFP@R-Lip. (**E**) Finite element analysis of acoustic field distribution. (**F**) PFP@R-Lip uptake by HCCLM3 cells via confocal microscopy (scale bar = 100 μm, all images were captured under the same magnification). (**G**) PFP@R-Lip uptake by HCCLM3 cells via Flow Cytometry and (**H**) relevant statistical analysis. $^{*}p < 0.05$, and $^{**}p < 0.01$.

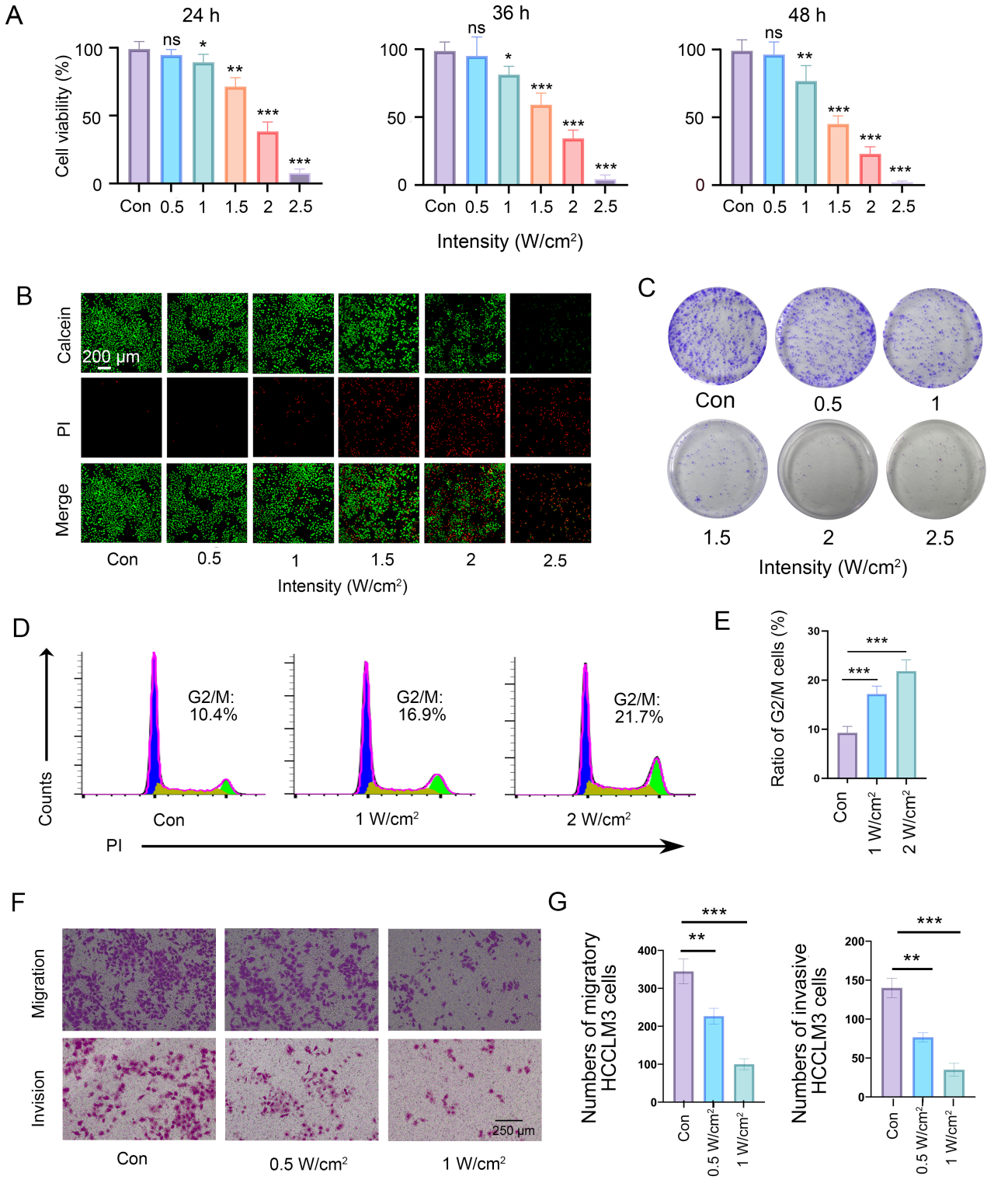

Fig. 2. Inhibitory effect of LIPUS combined with PFP@R-Lip on HCCLM3 cells. (**A**) MTT assay, (**B**) Calcein-AM/PI staining, and (**C**) colony formation assay irradiated by different LIPUS intensities combined with PFP@R-Lip (scale bar = 200 μm, all images were captured under the same magnification). (**D**) Cell cycle analysis and (**F**) Transwell assay (scale bar = 250 μm, all images were captured under the same magnification) irradiated by different LIPUS intensities combined with PFP@R-Lip and (**E, G**) relevant statistical analysis. ns: no significance, $^{*}p < 0.05$, $^{**}p < 0.01$ and $^{***}p < 0.001$.

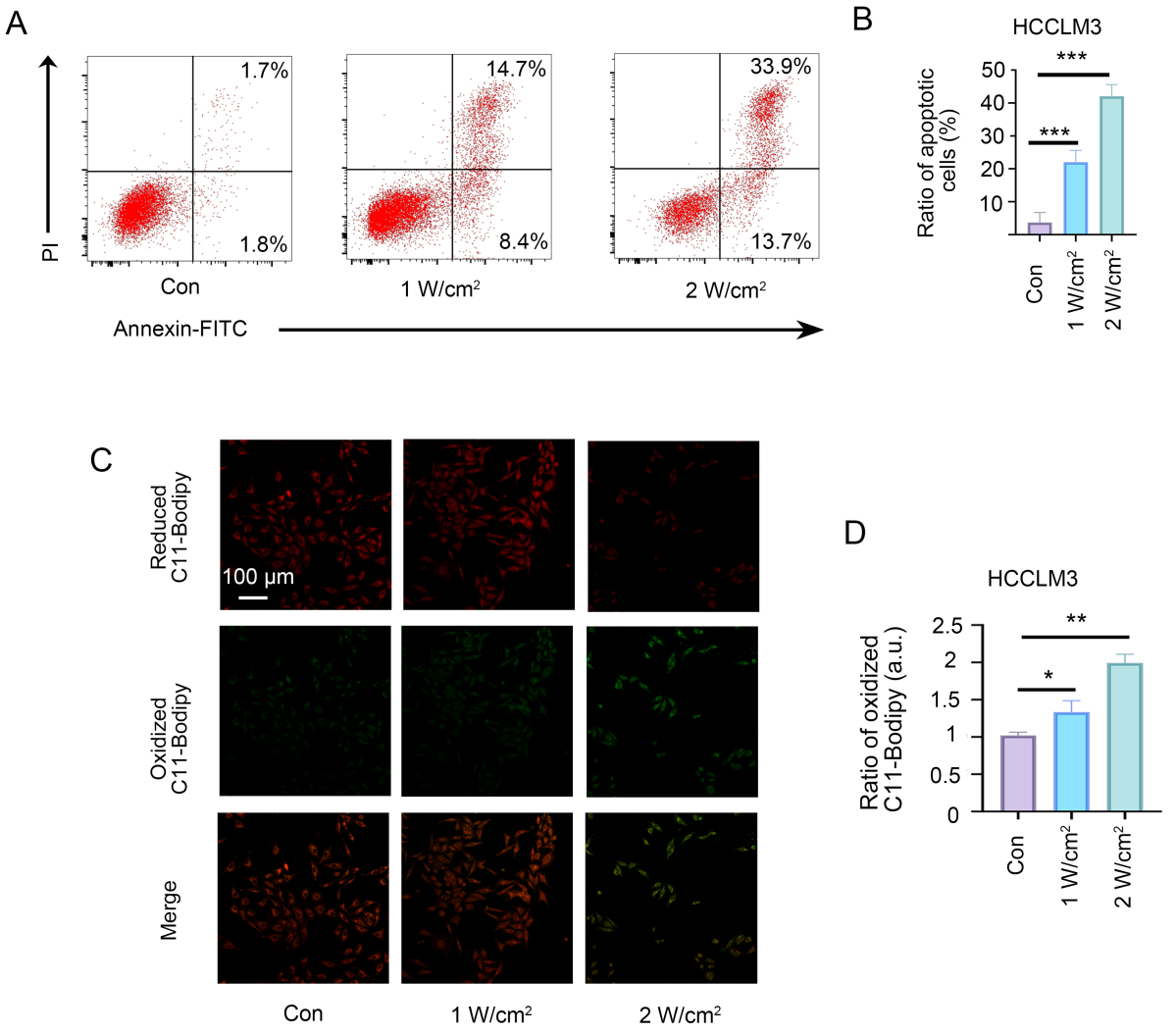

Fig. 3. Apoptosis and lipid peroxidation induced by LIPUS combined with PFP@R-Lip. (**A**) HCCLM3 cell apoptosis and (**C**) lipid peroxidation (scale bar = 100 μm, all images were captured under the same magnification) induced by different LIPUS intensities combined with PFP@R-Lip and (**B, D**) relevant statistical analysis. $^{*}p < 0.05$, $^{**}p < 0.01$ and $^{***}p < 0.001$.

LIPUS Combined With PFP@R-Lip Induces Apoptosis and Lipid Peroxidation in HCCLM3 Cells

Flow cytometry revealed LIPUS combined with PFP@R-Lip caused an intensity-dependent increase in the number of Annexin V-FITC-positive cells, confirming this combination induced apoptosis in HCCLM3 cells (Fig. 3**A**). Statistical analysis indicated compared with Con (apoptosis rate: 3.5 ± 2.7%), the apoptosis rate of HCCLM3 cells increased to 21.6 ± 3.8% and 42.9 ± 3.4% following treatment with LIPUS at 1 W/cm^2 and 2 W/cm^2 combined with PFP@R-Lip, respectively (Fig. 3**B**). Based on the C11-Bodipy staining, cells in the Con group exhibited predominantly red fluorescence (reduced C11-Bodipy), indicating a low basal level of lipid peroxidation. With the increase in LIPUS acoustic intensity (1 W/cm^2 and 2 W/cm^2), the green fluorescence (oxidized C11-Bodipy) was significantly enhanced, accompanied by a corresponding reduction in red fluorescence, which indicated the accumulation of lipid peroxidation products (Fig. 3**C**). Quantitative analysis showed the proportion of oxidized cells increased to approximately 1.3-fold and 1.9-fold of that in the Con group after treatment with LIPUS at 1 W/cm^2 and 2 W/cm^2 combined with PFP@R-Lip, respectively (Fig. 3**D**).

Transcriptomics Sequencing

Transcriptomics sequencing was performed to identify differentially expressed genes (DEGs) and associated signaling pathways in response to LIPUS combined with PFP@R-Lip. The Heatmap and Volcano map revealed that LIPUS combined with PFP@R-Lip significantly modulated a substantial number of DEGs, with 548 upregulated genes and 364 downregulated genes (Fig. 4**A**–**B**). Furthermore, KEGG enrichment analysis implied a significant im-

pact of LIPUS combined with PFP@R-Lip on the calcium ion signaling pathway (Fig. 4**C**).

Overexpression of Piezo1 in HCC and Poor Clinical Prognosis

To evaluate the clinical relevance of Piezo1 in HCC, we integrated transcriptomic profiles with clinical information from the Cancer Genome Atlas (TCGA) database. Bioinformatic analysis revealed upregulation of Piezo1 mRNA (gene symbol: FAM38A) in HCC tissues compared with adjacent normal controls (Fig. 4**D**). While no stage-dependent differential expression was observed across tumor progression stages (Fig. 4**F**). Fig. 4**E** indicated the correlation between elevated Piezo1 expression and reduced overall survival rates (log-rank $p < 0.05$). Complementary experimental validation demonstrated consistent protein-level overexpression of Piezo1 in HCCLM3 cells relative to normal hepatocytes (WRL68), as evidenced by immunofluorescence microscopy (Fig. 4**G**) and western blot quantification (Fig. 4**H**–**I**).

Piezo1 Knockdown

siPiezo1 (**Supplementary Table 1**) was designed and successfully transfected, with knockdown efficiency confirmed by Western blot (**Supplementary Fig. 7**). siPiezo1#2 exhibited a knockdown efficiency of approximately 83% and was used for subsequent experiments.

LIPUS Combined With PFP@R-Lip Induced Calcium Overload, MMP Depolarization and Apoptosis via Piezo1 Activation

Calcium ion levels were detected using the Fluo-4 AM fluorescence probe. Compared with the control (G1), pretreatment with the Piezo1 inhibitor GsMTx4 (G2) caused a slight reduction of Fluo-4 AM fluorescence in HCCLM3 cells, with no statistical significance. LIPUS combined with PFP@R-Lip (G3) led to a marked enhancement of intracellular calcium ion, and the fluorescence intensity was approximately 4.2-fold higher than that in G1. Notably, the intracellular calcium ion concentration was partially reversed by GsMTx4 in the G4 (Fig. 5**A** and **Supplementary Fig. 8**). Piezo1 knockdown induced a similar pattern of intracellular calcium alteration as GsMTx4 pretreatment (**Supplementary Fig. 9**). MMP depolarization was assessed using the JC-1 fluorescent probe. Compared with the control (G1), pretreatment with GsMTx4 (G2) caused no significant change in MMP. In LIPUS combined with PFP@R-Lip group (G3), JC-1 monomers (green fluorescence) exhibited a marked predominance over JC-1 aggregates (red fluorescence). The ratio of JC-1 monomers to aggregates in G3 was approximately 2.1-fold of that in G1. Notably, the predominance of JC-1 monomers was partially reversed by GsMTx4 in the G4 (Fig. 5**B** and **Supplementary Fig. 10**). Piezo1 knockdown induced a similar pattern of MMP alteration as GsMTx4 pretreatment (**Supplementary Fig. 11**). Apoptosis was detected via flow cytometry. The results showed the apoptosis rates of HCCLM3 cells were at low levels in G1 (5.3 ± 2.6%) and G2 (4.8 ± 3.6%), with no statistically significant difference. In contrast, the apoptosis rate in G3 was significantly elevated to 41.4 ± 9.3%. Whereas in G4, the apoptosis rate was reduced to 33.4 ± 4.7% (Fig. 5**C**–**D**). Piezo1 knockdown induced a similar pattern of apoptosis as GsMTx4 pretreatment (**Supplementary Fig. 12**). Western blot analysis of apoptosis-related proteins revealed no statistically significant differences in the expression of Bcl-2, Bax, and cleaved Caspase-3 between G1 and G2. In contrast, LIPUS (G3) significantly upregulated the expression of the pro-apoptotic proteins Bax and cleaved Caspase-3, while downregulating the anti-apoptotic protein Bcl-2. Additionally, the altered expression trends of these apoptosis-related proteins were partially reversed by GsMTx4 pretreatment (Fig. 5**E**–**F**).

LIPUS Combined With PFP@R-Lip Induced ROS Generation and Ferroptosis via Piezo1 Activation

Intracellular ROS level in HCCLM3 cells was detected using the DCFH-DA fluorescent probe. The results indicated ROS (green fluorescence) remained at low levels in both G1 and G2, with no statistically significant difference. In G3, ROS level in HCCLM3 was markedly enhanced, with the fluorescence intensity increased by approximately 3.0-fold compared with G1, indicating that LIPUS combined with PFP@R-Lip could significantly induce intracellular ROS generation. In G4, GsMTx4 partially reversed the LIPUS-induced elevation of ROS, with the fluorescence intensity reduced to approximately 50% of that in G3 (Fig. 6**A**–**B**). Piezo1 knockdown induced a similar pattern of intracellular ROS alteration as GsMTx4 pretreatment (**Supplementary Fig. 13**). Assessment of ferrous ion levels in HCCLM3 cells was performed using RhoNox-6 staining. No significant change in ferrous ion levels (red fluorescence) was observed between G1 and G2. In G3, red fluorescence increased significantly, with the average fluorescence intensity approximately 2.3 times of that in G1. This indicated the accumulation of ferrous ions, which is a hallmark event of ferroptosis. In G4, GsMTx4 partially alleviated the increased ferrous ion levels induced by LIPUS combined with PFP@R-Lip. The red fluorescence intensity decreased to about 66% of that in G3 (**Supplementary Fig. 14**). Assessment of lipid peroxidation in HCCLM3 cells was performed using C11-Bodipy staining. Results showed that in G1, the C11-Bodipy probe mainly exhibited reduced state (red fluorescence). In G2, the red fluorescence intensity showed no significant change. In G3, green fluorescence increased significantly, with the average fluorescence intensity approximately 1.8 times of that in G1. This indicated the accumulation of oxidized lipid components. In G4, GsMTx4 partially alleviated the lipid peroxidation induced by LIPUS

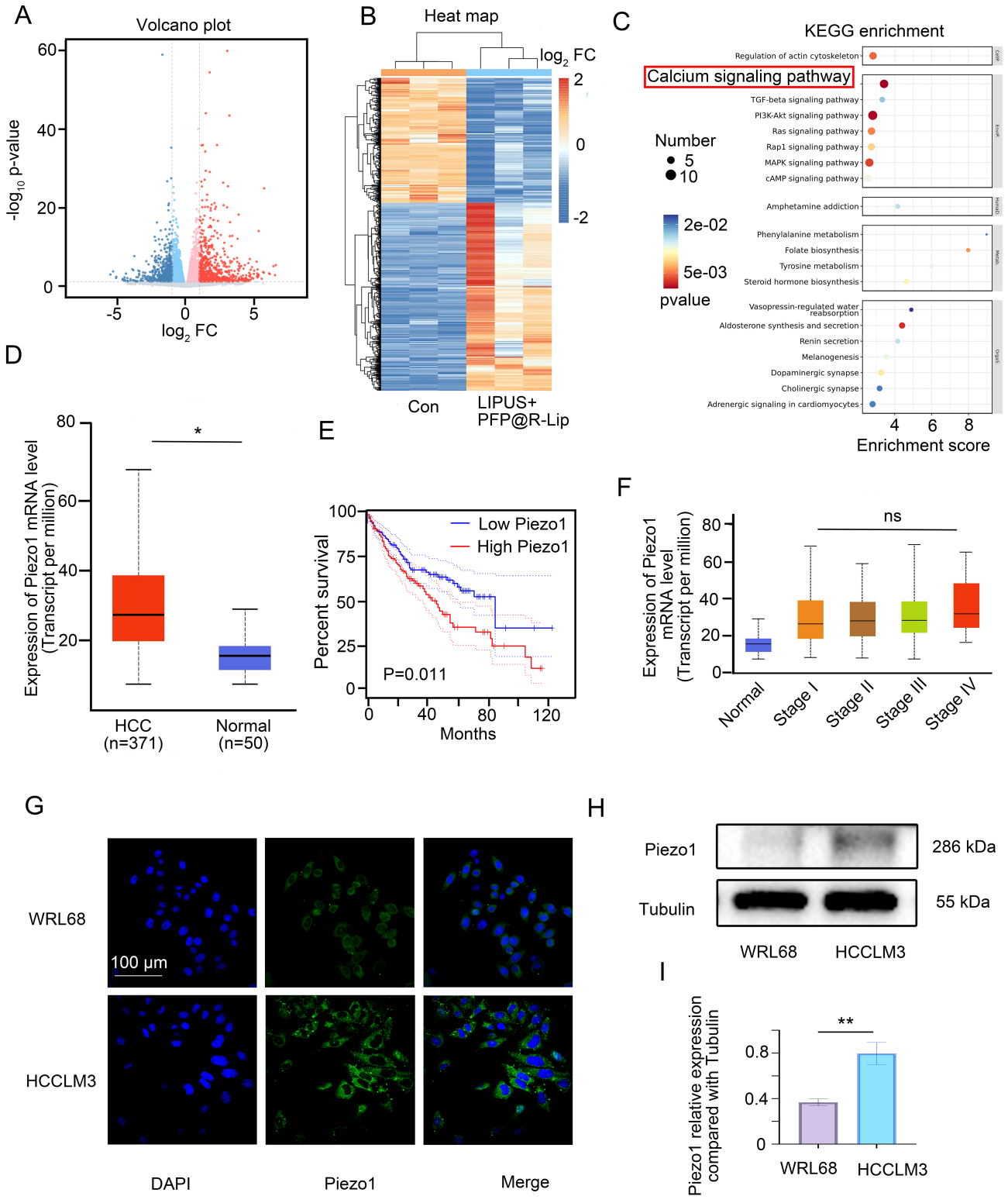

Fig. 4. Overexpression of Piezo1 in HCC and poor clinical prognosis. (**A**) Volcano plot and (**B**) heatmap of transcriptomics sequencing after LIPUS combined with PFP@R-Lip. (**C**) Calcium signaling pathway involvement is evidenced by KEGG enrichment. (**D**) Piezo1 mRNA levels in the TCGA database: HCC patients vs normal controls. (**E**) Overall survival analysis of HCC patients stratified by Piezo1 mRNA expression. (**F**) Piezo1 mRNA levels across HCC clinical stages. (**G**) Immunofluorescence (scale bar = 100 μm, all images were captured under the same magnification) and (**H** and **I**) Western blot analysis comparing Piezo1 expression in normal hepatocytes and HCC cells. ns: no significance, $^{*}p < 0.05$ and $^{**}p < 0.01$.

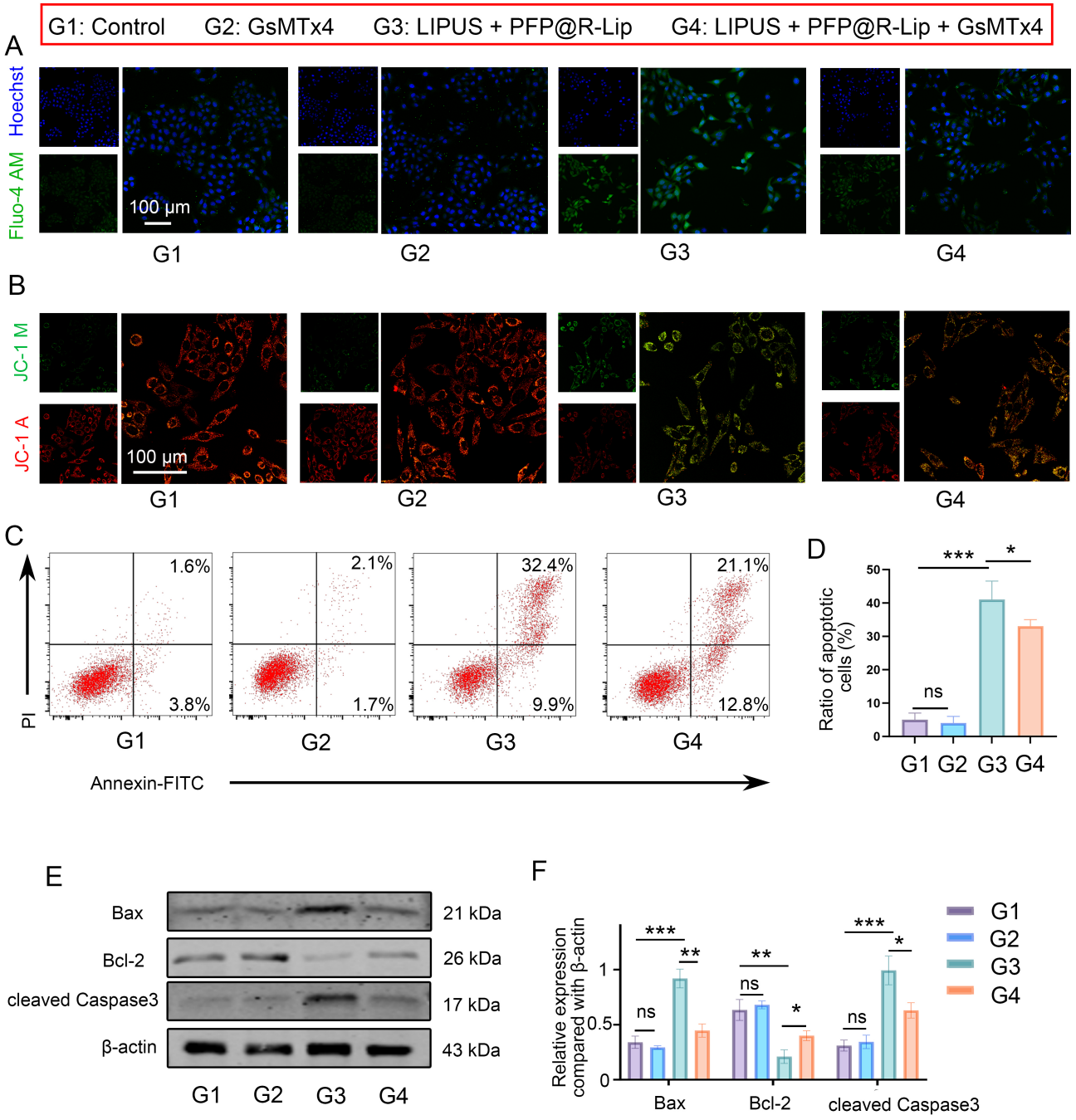

Fig. 5. Calcium overload, MMP depolarization, and apoptosis induced by LIPUS combined with PFP@R-Lip via Piezo1 activation. (**A**) Fluo-4 AM detection of intracellular calcium ion concentration in each group (scale bar = 100 μm, all images were captured under the same magnification). (**B**) JC-1 analysis of MMP depolarization in cells of each group (scale bar = 100 μm, all images were captured under the same magnification). (**C**) Flow cytometric analysis of cell apoptosis in each group and (**D**) relevant statistical analysis. (**E**) Expression of apoptosis-related proteins in each group and (**F**) relevant statistical analysis. ns: no significance, $^{*}p < 0.05$, $^{**}p < 0.01$ and $^{***}p < 0.001$.

combined with PFP@R-Lip. The content of oxidized C11-Bodipy decreased to about 76% of that in G3 (Fig. 6**C**–**D**). Piezo1 knockdown induced a similar pattern of lipid peroxidation as GsMTx4 pretreatment (**Supplementary Fig. 15**). Ferrostatin-1 rescue experiments further confirmed ferroptosis induced by LIPUS combined with PFP@R-Lip. Compared with G1, Ferrostatin-1 pretreatment (G7) did not significantly alter the fluorescence intensity of C11Bodipy. However, Ferrostatin-1 significantly attenuated the oxidized C11Bodipy fluorescence intensity induced by LIPUS + PFP@R-Lip in G8, with the average fluorescence intensity decreased to about 63% of that in G3 (**Supplementary Fig. 16**). Western blot analysis of ferroptosis-related proteins revealed that no statistically significant differences were observed in the expression of ACSL4, xCT, or GPX4 between G1 and G2. However, LIPUS combined with PFP@R-Lip (G3) significantly upregulated the expression of ACSL4 (a protein that promotes lipid peroxidation) while downregulating the expression of xCT and GPX4, both of which inhibit lipid peroxidation. Moreover, these changes in ferroptosisrelated protein expression could be partially reversed by pretreatment with GsMTx4 in G4 (Fig. 6**E**–**F**). These findings collectively confirmed that LIPUS combined with PFP@R-Lip induced ROS generation and ferroptosis in HCCLM3 through Piezo1 activation.

LIPUS Combined With PFP@R-Lip Induced Calreticulin (CRT) Translocation via Piezo1 Activation

Immunofluorescence results showed that, compared with G1, the fluorescence intensity of CRT on HCCLM3 cells in G2 showed no significant difference. In G3, green fluorescence increased significantly, which was approximately 2.7 times of that in G1. While in G4, the green fluorescence of GsMTx4 pretreated cells reduced to 66% of that in G3 (Fig. 7**A** and **Supplementary Fig. 17**). Flow cytometry analysis of CRT exposure on the cell membrane yielded results consistent with the aforementioned findings. Compared with G1, the number of CRT-positive HCCLM3 cells in G2 showed no significant difference. However, the CRT fluorescence signal exhibited a significant rightward shift in G3, which was approximately 2.4-fold of that in G1. In G4, after pretreatment with GsMTx4, the CRT signal on cells shifted leftward compared with G3, indicating suppressed CRT translocation to the membrane (Fig. 7**B** and **Supplementary Fig. 18**). These results confirmed LIPUS combined with PFP@R-Lip induced translocation of CRT to the membrane, an effect that can be partially reversed by inhibiting the Piezo1 channel.

LIPUS Combined With PFP@R-Lip Promoted the Release of HMGB1 and ATP via Piezo1 Activation

ELISA results showed the level of HMGB1 in the supernatant of HCCLM3 cells was 65.4 ± 15.3 ng/mL in G1. In G2, HMGB1 level was 72.4 ± 23.6 ng/mL. Statistical analysis indicated no significant difference in HMGB1 release between G1 and G2. In G3, HMGB1 concentration significantly increased to 281.5 ± 39.3 ng/mL after LIPUS combined with PFP@R-Lip. In G4, the HMGB1 level was partially reversed to 243.7 ± 42.3 ng/mL by pretreating with GsMTx4 (Fig. 7**C**). ATP assay revealed that ATP concentration in the supernatant of HCCLM3 was 5.6 ± 1.3 nM in G1. In G2, ATP level was 6.1 ± 2.4 nM with no significant difference from that in G1. After LIPUS (G3) intervention, ATP concentration rose significantly to 21.5 ± 6.6 nM. In G4, ATP release was attenuated to 17.2 ± 5.7 nM by pretreating with GsMTx4 (Fig. 7**D**).

Increased accumulation of PFP@R-Lip in tumors

At 9 h following intravenous administration of DiI/PFP@R-Lip or DiI/PFP@Lip into tumorbearing mice, the fluorescent signals were primarily detected in the liver, kidneys, and tumor tissues. And mice injected with the targeted formulation (DiI/PFP@R-Lip) exhibited strong fluorescence signals in the tumor region at 9 h postinjection, whereas only weak signals were detected in the tumors of mice receiving nontargeted DiI/PFP@Lip (**Supplementary Fig. 19A**–**B**). Quantitative analysis confirmed about 1.7 times higher radiant efficiency in the targeted group than the non-targeted group, indicating improved tumor targeting mediated by cRGD modification (**Supplementary Fig. 19C**).

LIPUS Combined With PFP@R-Lip Suppressed Subcutaneous Tumor via Piezo1 Activation

Fig. 8**A** illustrates the experimental timeline for treating C57BL/6 mice. Mice bearing subcutaneous tumors were randomly divided into four groups: mG1, mG2, mG3, and mG4. Body weight changes of the mice over 21 days after the first intervention were shown in Fig. 8**B**. No significant differences in body weight were observed among the groups on day 21. And, no obvious toxicity or organ damage was observed in the major organs of mice in each group on day 21 (**Supplementary Fig. 20**). Fig. 8**C** presented images of tumors resected from each group after the mice were euthanized on day 21. Tumor volume and weight changes were displayed in Fig. 8**D** and 8**E**. No significant difference in tumor volume and weight was observed between mG1 and mG2. In contrast, tumors in mG3 were significantly inhibited. This tumorsuppressive effect was partially reversed by GsMTx4 in mG4. Fig. 8**F** showed the histological analysis of the tumors. H&E staining revealed that tumor cells in both mG1 and mG2 were arranged densely with higher nuclear-to-cytoplasmic ratios, and no obvious necrotic areas were observed. In contrast, tumor tissues in mG3 exhibited looser and more disordered cell arrangement, with noticeably enlarged intercellular spaces and regional structural disruption. The administration of GsMTx4 (mG4) partially reversed these alterations. Ki67 staining showed no significant difference in the number of Ki67-positive cells between mG1 and mG2.

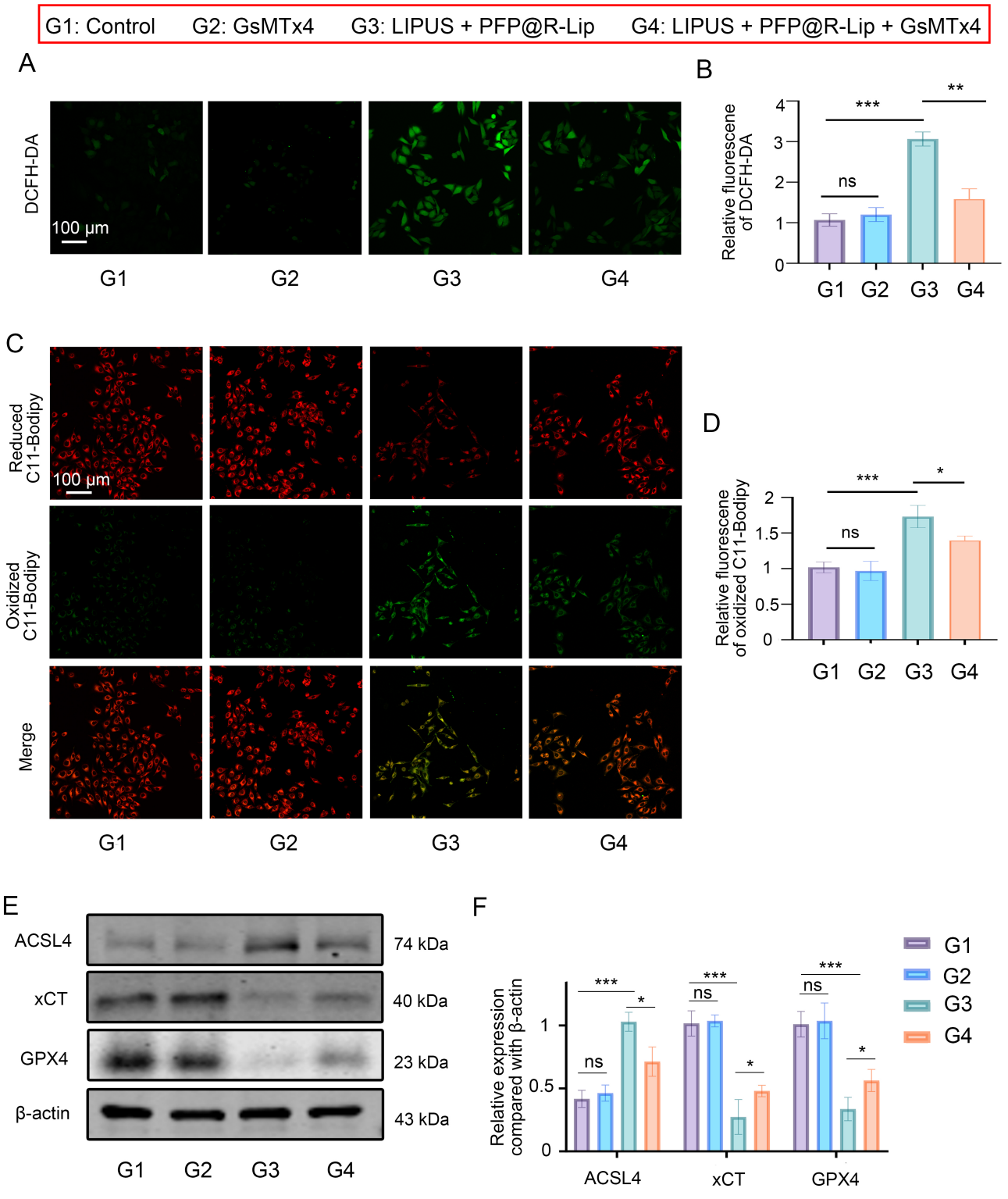

Fig. 6. ROS generation and ferroptosis induced by LIPUS combined with PFP@R-Lip via Piezo1 activation. (**A**) DCFH-DA detection of intracellular ROS generation in each group (scale bar = 100 μm, all images were captured under the same magnification) and (**B**) relevant statistical analysis. (**C**) C11-Bodipy analysis of intracellular lipid peroxidation in each group (scale bar = 100 μm, all images were captured under the same magnification) and (**D**) relevant statistical analysis. (**E**) Expression of ferroptosis-related proteins and (**F**) relevant statistical analysis. ns: no significance, $^{*}p < 0.05$, $^{**}p < 0.01$ and $^{***}p < 0.001$.

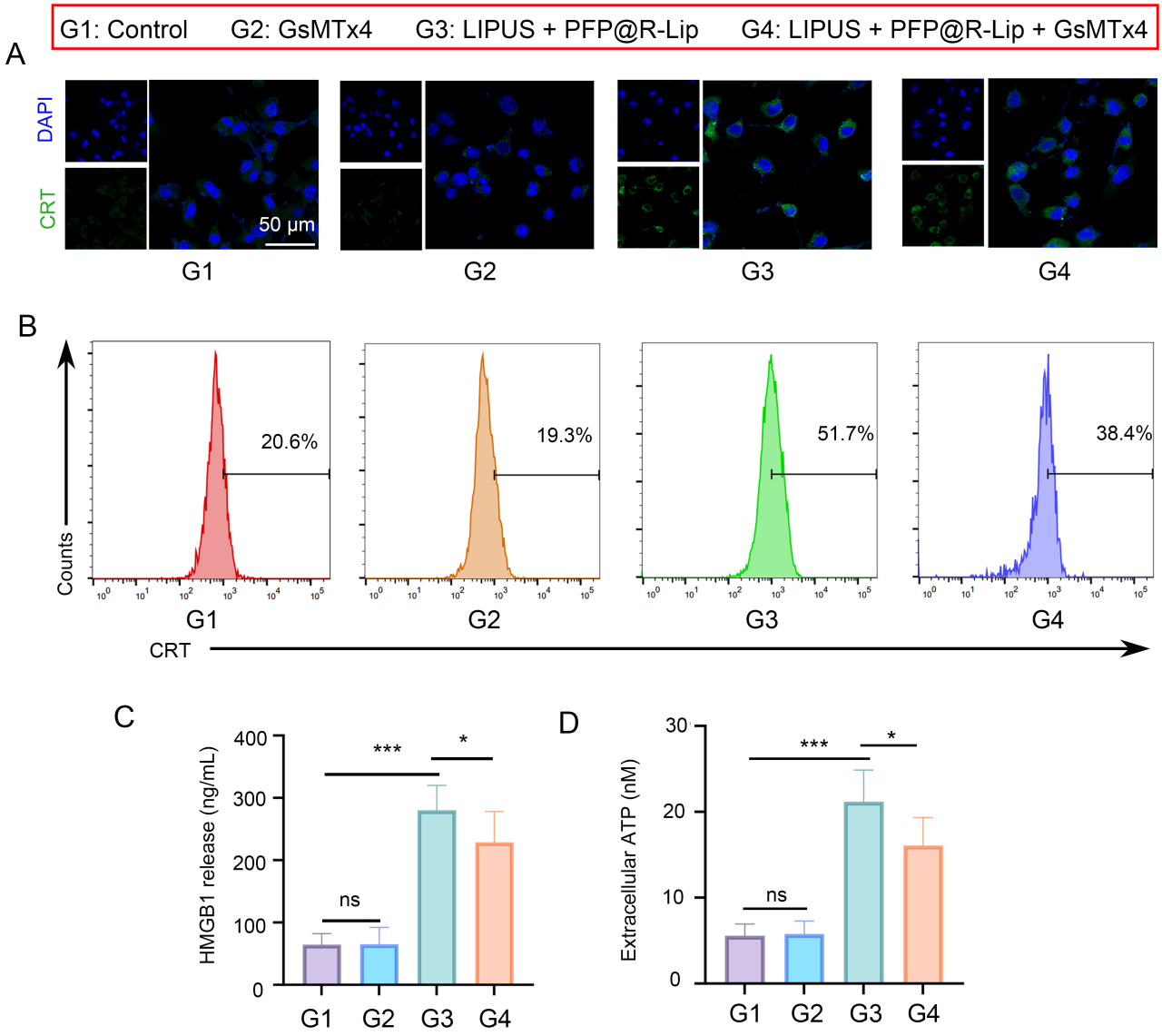

Fig. 7. Increase of DAMPs induced by LIPUS combined with PFP@R-Lip via Piezo1 activation. (**A**) Immunofluorescence (scale bar = 50 μm, all images were captured under the same magnification) and (**B**) flow cytometry analysis of CRT exposure in each group. (**C**) HMGB1 and (**D**) ATP levels in the cell supernatant of each group. ns: no significance, $^{*}p < 0.05$ and $^{***}p < 0.001$.

However, mG3 displayed a significant reduction in Ki67-positive cells within tumor tissues, which could be partially reversed by GsMTx4 pretreatment (mG4). TUNEL assay confirmed enhanced apoptosis in mG3, an effect that was attenuated by inhibition of Piezo1 (mG4). The expression levels of the antioxidant markers xCT and GPX4 showed no significant difference between mG1 and mG2. Compared with mG1, LIPUS combined with PFP@R-Lip (mG3) significantly downregulated the expression of xCT and GPX4, and this downregulation could be partially reversed by GsMTx4 pretreatment (mG4). As for the pro-lipid peroxidation marker ACSL4, its expression was upregulated in mG3 compared with mG1, and this upregulation was also reversed in mG4.

LIPUS Combined With PFP@R-Lip Improved Antitumor Immunity via Piezo1 Activation

In tumor tissues, the proportion of mature DCs expressing $CD80^{+}$ and $CD86^{+}$ was 6.7 ± 3.1% in mG1 and 7.9 ± 4.4% in mG2, with no significant difference. mG3 exhibited a significantly increased percentage of mature DCs (28.4 ± 2.2%), while mG4 showed a partial reduction to 19.8 ± 2.4%. This indicates that GsMTx4 treatment partly suppressed DC maturation induced by LIPUS combined with PFP@R-Lip. A similar trend was observed in splenic DCs: mG1 with 9.7 ± 2.6% mature DCs, mG2 with 12.4 ± 3.4%, mG3 with 32.4 ± 5.2%, and mG4 with 24.8 ± 4.4% (Fig. 9**A**–**B**). Flow cytometry analysis of TAM polarization revealed that the proportion of $F4/80^{+}CD206^{+}$

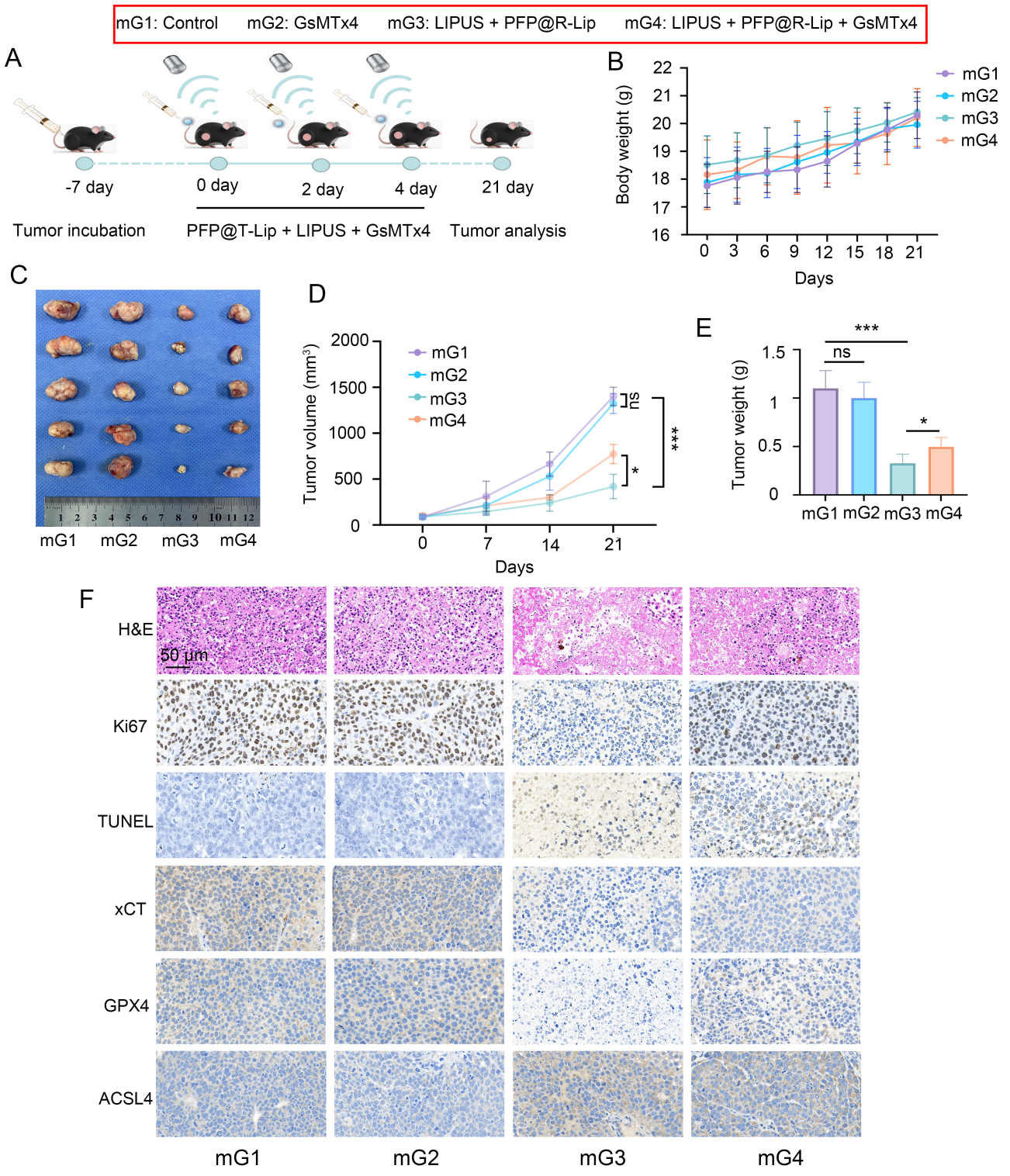

Fig. 8. *In vivo* antitumor effect induced by LIPUS combined with PFP@R-Lip via Piezo1 activation. (**A**) Procedures of the *in vivo* experiments. (**B**) Mice's body weight changes in each group. (**C**) Images of the dissected tumors from each group. Statistical analysis of (**D**) tumor volume and (**E**) weight in each group. (**F**) Staining of tumor sections in each group (scale bar = 50 μm, all images were captured under the same magnification). ns: no significance, $^{*}p < 0.05$ and $^{***}p < 0.001$.

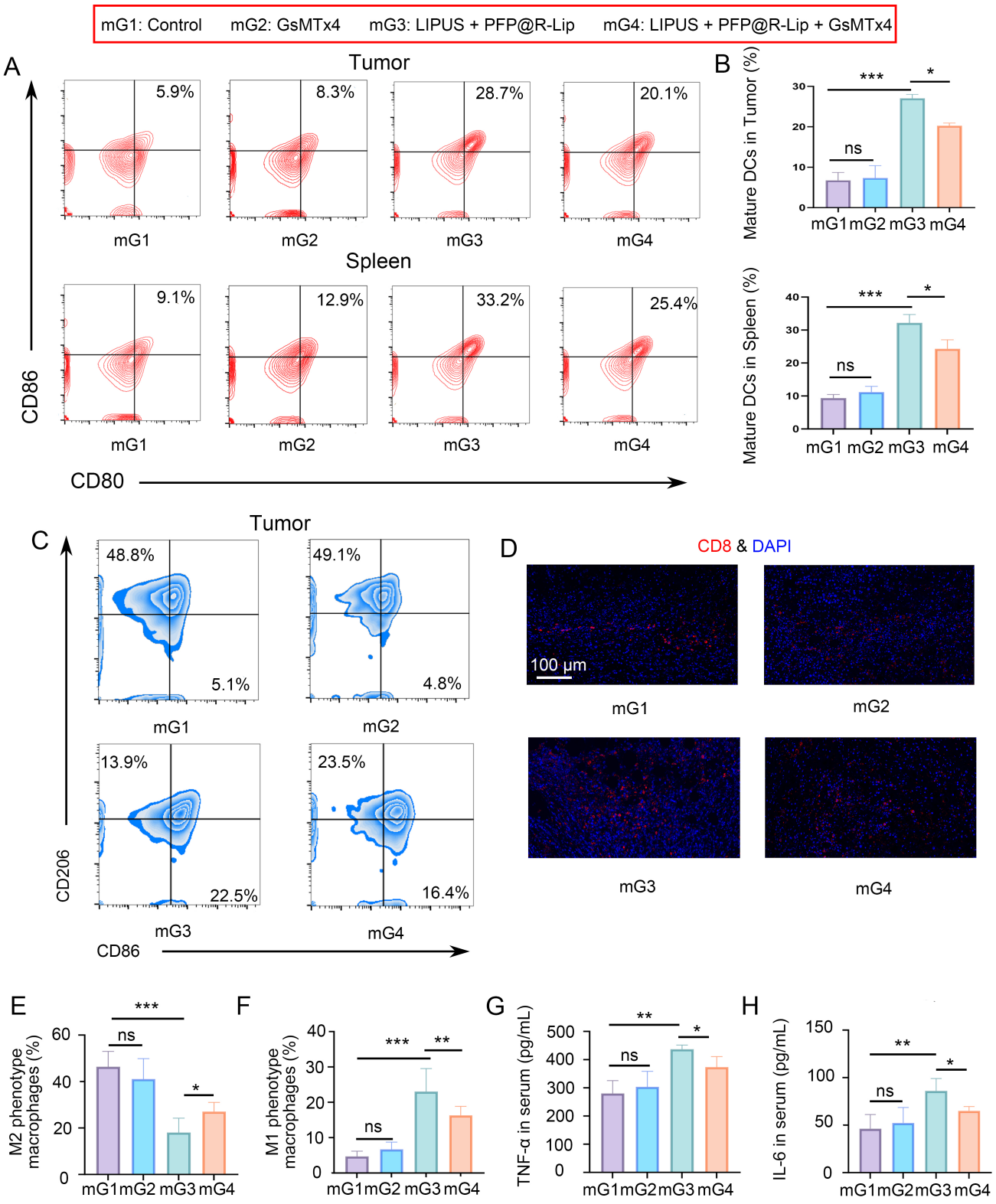

Fig. 9. Antitumor immunity improved by LIPUS combined with PFP@R-Lip via Piezo1 activation. (**A**) Flow cytometric analysis of DCs maturation in tumors and spleens of each group and (**B**) relevant statistical analysis. (**C**) Flow cytometric analysis of TAMs polarization in tumors of each group. Statistical analysis of the proportions of (**E**) M2 and (**F**) M1 phenotype TAMs. (**D**) Immunofluorescence analysis of $CD8^+$ cell infiltration at the tumor margin (scale bar = 100 μm, all images were captured under the same magnification). (**G**) TNF-α and (**H**) IL-6 levels in the serum of each group. ns: no significance, $^*p < 0.05$, $^{**}p < 0.01$ and $^{***}p < 0.001$.

M2-type TAMs was 48.3 ± 8.7% in the mG1 and 42.9 ± 11.4% in mG2, with no significant change. mG3 showed a significant decrease to 16.9 ± 8.2%, which was partially reversed in mG4 (24.8 ± 5.4%). Conversely, the percentage of F4/80$^+$CD86$^+$ M1-type TAMs was 5.3 ± 1.7% in mG1 and 7.7 ± 2.4% in mG2. LIPUS combined with PFP@R-Lip (mG3) significantly increased this proportion to 22.9 ± 7.2%, while the combination with GsMTx4 (mG4) led to a partial reversal (15.8 ± 3.4%), demonstrating that GsMTx4 could attenuate both the reduction in M2-type TAMs and the increase in M1-type TAMs induced by LIPUS combined with PFP@R-Lip (Fig. 9**C** and **E**–**F**). Immunofluorescence staining of tumor sections indicated low levels of CD8$^+$ T cell infiltration at the tumor margins in both mG1 and mG2, with no significant difference in mean fluorescence intensity. In mG3, CD8$^+$ T cell infiltration was markedly increased, with the MFI rising to approximately 2.8 times of that in mG1. Whereas in mG4, the mean fluorescence intensity was reduced to about 71% of the mG3 level (Fig. 9**D** and **Supplementary Fig. 21**). Furthermore, ELISA measurements of serum cytokine levels showed that TNF-α concentrations were 281 ± 35 pg/mL in mG1, 298 ± 37 pg/mL in mG2, 423 ± 15 pg/mL in mG3, and 379 ± 26 pg/mL in mG4 (Fig. 9**G**). IL-6 levels were 48 ± 11 pg/mL in mG1, 52 ± 8 pg/mL in mG2, 84 ± 9 pg/mL in mG3, and 61 ± 4 pg/mL in mG4 (Fig. 9**H**).

Discussion

HCC is the sixth most commonly diagnosed cancer and the third leading cause of cancer-related mortality globally, with an increasing mortality rate worldwide [1]. The highly complex immunosuppressive tumor microenvironment and inadequate targeting precision of clinical therapeutic modalities are the main causes of the limited efficacy and severe adverse effects of conventional HCC therapies [17]. This study prepared c-RGD-modified targeted liposomes, PFP@R-Lip, with a hydrodynamic diameter of 243.1 ± 79.3 nm, a surface potential of -16.6 ± 4.1 mV, a spherical morphology, and favorable stability. Their negative surface potential effectively prevents aggregation and precipitation through electrostatic repulsion. And their small size facilitates passive targeting via the Enhanced Permeability and Retention (EPR) effect, leveraging the larger interendothelial gaps within tumor tissues [18]. Furthermore, previous studies have indicated that the c-RGD cyclic peptide on PFP@R-Lip enables precise active targeting to integrin receptors overexpressed on cancer cells, which is in line with our observations [19,20]. Finite element analysis simulating the ultrasound field distribution demonstrated that LIPUS exhibits excellent acoustic focusing ability. The synergy of passive and active targeting of PFP@R-Lip significantly promoted its accumulation in HCC, and the combination of this targeting property with the acoustic focusing effect of LIPUS further improved the spatial precision of therapy. Upon LIPUS irradiation, the PFP core within PFP@R-Lip undergoes a liquid-to-gas phase transition, which is able to increase the acoustic contrast with adjacent tissues during ultrasound imaging. This allows for the visual monitoring of PFP@R-Lip targeting, consistent with findings from previous studies [21,22]. Additionally, the formed gas nucleus can serve as a cavitation core for LIPUS, which reduces the cavitation threshold. This allows LIPUS to exert stronger cavitation effects at lower acoustic intensities [23], thus minimizing mechanical and thermal damage to adjacent tissues. However, it should be noted that a higher acoustic intensity is not necessarily advantageous. As demonstrated in Fig. 1**D**, excessively high acoustic intensity (3 W/cm^2) with prolonged duration (2 min) can induce the rupture of PFP@R-Lip, thereby deteriorating the ultrasound imaging performance. Therefore, an optimal acoustic intensity range is critical to harness the benefits of phase transition and cavitation while avoiding particle destruction. Accumulating evidence has shown that the mechanical properties of the HCC microenvironment are involved in tumor cell initiation and progression [24]. In this context, physical therapeutic modalities such as LIPUS have attracted increasing attention due to their unique advantages in cancer treatment. LIPUS delivers mechanical energy precisely through non-thermal bioeffects (cavitation and acoustic radiation force) which have presented antitumor effects in various cancer cell types [25,26]. However, the specific molecular mechanisms underlying its antitumor effects in HCC have not been fully elucidated to date. This study confirmed that LIPUS combined with PFP@R-Lip inhibits the viability, proliferation, cell cycle, migration and invasion of HCCLM3 cells. To elucidate the key molecular mechanisms underlying the inhibition of HCC by LIPUS combined with PFP@R-Lip, transcriptome sequencing was performed indicating a large number of differentially expressed genes and involvement of calcium signaling pathways.

Piezo1, a novel mechanosensitive ion channel, could transform mechanical stimuli into biochemical signals by mediating calcium influx, playing a key role in tumorigenesis, metastasis, and microenvironment regulation [27]. Numerous studies have demonstrated that mechanical stimuli such as ultrasound can activate the Piezo1 channel, leading to an increase in intracellular calcium ion levels [10,12,28]. Based on these findings, we hypothesized that LIPUS combined with PFP@R-Lip exerted anti-HCC effects by activating Piezo1 channel and modulating calcium ion signaling pathways. Bioinformatic analysis of The Cancer Genome Atlas database revealed that Piezo1 mRNA (gene symbol: FAM38A) expression is significantly upregulated in HCC tissues compared with adjacent normal liver tissues. However, no statistical difference was observed between tumor stages. Moreover, Piezo1 overexpression is significantly associated with shorter overall survival in HCC patients, suggesting it may serve as an important molecular driver in HCC development. Immunofluorescence and

Western blot assays further confirmed Piezo1 overexpression in HCCLM3 cells, validating its feasibility as a therapeutic target. This study found that LIPUS combined with PFP@R-Lip induced intracellular calcium overload in HCCLM3 cells, leading to mitochondrial dysfunction and apoptosis. And these effects were partially reversed by the Piezo1 channel inhibitor GsMTx4.

Calcium ions are also important regulators of cell membrane damage and ferroptosis [29,30]. Ferroptosis is an iron-dependent form of regulated cell death triggered by the accumulation of lipid peroxides. The core mechanisms of ferroptosis involve lipid peroxidation, imbalance of antioxidant systems, and dysregulation of iron metabolism [31]. Intracellular GPX4 and its upstream regulator xCT play crucial roles in maintaining redox balance. However, it remains unclear whether calcium fluxes during ferroptosis are transmitted through cell membrane channels, endogenous channels, or through damaged regions of the plasma membrane. Furthermore, how these fluxes collectively contribute to overall changes in cellular calcium homeostasis remains to be elucidated [32]. Increased intracellular calcium concentration has been reported to inhibit ferroptosis [33]. However, excessive calcium accumulation in the cytoplasm may induce ferroptosis, partly because mitochondrial calcium homeostasis is crucial for regulating mitochondrial energy metabolism. Impaired mitochondrial metabolism can generate excess ROS, thereby promoting ferroptosis [34,35]. This study proved LIPUS combined with PFP@R-Lip could induce intracellular calcium overload by activating the Piezo1 channel, increase mitochondrial permeability, generate ROS, and initiate a chain reaction of membrane lipid peroxidation. Simultaneously, it inhibits the expression of antioxidant molecules xCT and GPX4 and upregulates the pro-oxidant molecule ACSL4, disrupting glutathione synthesis and the detoxification of lipid peroxides. However, the specific molecular mechanisms by which calcium overload regulates the expression of xCT, GPX4, and ACSL4 require further investigation. This effect on mitochondrial membrane integrity and cellular antioxidant defense systems, together with the induction of apoptotic cell death, exerts a dual lethal effect on HCC cells. This may potentially circumvent tumor cell resistance to a single cell death pathway.

ICD has emerged as a research focus in the field of tumor immunotherapy in recent years. However, traditional ICD-inducing strategies (e.g., chemotherapy, photodynamic therapy) are limited by low induction efficiency, blockage by the immunosuppressive microenvironment, and inadequate tumor-targeting precision, greatly limiting the clinical application of ICD [36]. The precise targeting and induction of intracellular calcium homeostasis imbalance by LIPUS combined with PFP@R-Lip provides a promising solution to these problems. Calcium signaling disruption triggered by Piezo1 activation is one of the key triggers for ICD initiation [37]. Moreover, apoptosis and ferroptosis resulting from calcium signaling disruption can also effectively drive tumor cells to undergo ICD [15,38]. The results of this study also indicated that LIPUS combined with PFP@R-Lip could significantly induce CRT translocation to the cell membrane, promote the release of HMGB1 and ATP, recruit and activate DCs, thereby initiating subsequent specific T-cell immune responses. Furthermore, LIPUS was able to promote the repolarization of TAMs towards the M1 phenotype within tumor tissue, thereby improving the immunosuppressive microenvironment and enhancing ICD effects. The study also found increased infiltration of $CD8^+$ T cells at the tumor margin and elevated levels of the antitumor cytokines TNF-α and IL-6 in mouse serum following LIPUS intervention. These results demonstrate that LIPUS can improve the immune response against HCC. GsMTx4 was able to partially reverse these effects, proving the pivotal role of the Piezo1 channel. However, this study has several limitations. First, the potential contribution of Piezo1 on immune cells cannot be ruled out, requiring conditional knockout or coculture studies. Second, blood routine and liver/kidney function tests were not performed. Serum biochemistry and hematology analyses are needed for safety confirmation. Third, Yoda1 and Ca^{2+} chelation experiments were absent, limiting full causal establishment of Piezo1mediated calcium signaling, although genetic knockdown and GsMTx4 inhibition already support Piezo1 necessity. Fourth, vaccination-rechallenge assays were not performed. Definitive demonstration of immunological memory remains to be established despite observed DAMP release, DC maturation, TAM repolarization, $CD8^+$ T cell infiltration, and cytokine elevation. All the limitations should be addressed in future work.

Conclusions

In this study, a cRGDmodified targeted liposomal formulation (PFP@R-Lip) was successfully prepared. When combined with LIPUS, PFP underwent a liquidtogas phase transition, enabling ultrasound imaging. This combination appeared to activate Piezo1, leading to calcium overload, mitochondrial depolarization, ROS accumulation, and lipid peroxidation. These events may synergistically induce apoptosis and ferroptosis in HCC cells, accompanied by DAMP release, DC maturation, $CD8^+$ T cell infiltration, and TAM repolarization. Collectively, these findings provide a theoretical basis for the combination of LIPUS and PFP@R-Lip in HCC treatment, though additional mechanistic and translational studies are needed.

Availability of Data and Materials

The datasets used and/or analyzed during the current study are available from the corresponding author on reasonable request.

Author Contributions

JJ was responsible for writing the original draft, methodology, investigation, data curation and formal analysis; XLD, WDW, MML, YXM, MWZ, LLH and JMN conducted investigation and data curation; XHY contributed to writing review & editing, supervision, project administration and conceptualization. All authors read and approved the final manuscript. All authors agree to be accountable for all aspects of the work in ensuring that questions related to the accuracy or integrity of any part of the work are appropriately investigated and resolved.

Ethics Approval and Consent to Participate

The animal experimental protocol was approved by the Animal Ethics Committee of the First Affiliated Hospital of Harbin Medical University (Approval No. 2024052) and all of the participants provided signed informed consent.

Acknowledgments

Not applicable.

Funding

This study was financially supported by the National Natural Science Foundation of China (grant numbers 82272000, 82272053) and Scientific Research & Innovation Foundation of the First Affiliated Hospital of Harbin Medical University (grant number 2024M20).

Conflict of Interest

The authors declare no conflict of interest.

Supplementary Material

Supplementary material associated with this article can be found, in the online version, at https://doi.org/10.22203/eCM.v057a06.

References

[1] Singal AG, Kanwal F, Llovet JM. Global trends in hepatocellular carcinoma epidemiology: implications for screening, prevention and therapy. Nat Rev Clin Oncol. 2023; 20: 864–884. https://doi.org/10.1038/s41571-023-00825-3.

[2] Matsushita M, Moriwaki M. Autophagy Modulates Immunogenic Cell Death in Cancer. Cancers. 2026; 18: 205. https://doi.org/10.3390/cancers18020205.

[3] Lei K, Chen J, Deng Y, Peng Y, Zhai X, Ren X, *et al*. Cracking the code of cancer immunotherapy resistance: emerging roles of pyroptosis and necroptosis. Journal of Experimental & Clinical Cancer Research: CR. 2025; 44: 308. https://doi.org/10.1186/s13046-025-03569-3.

[4] Morioka S, Maueröder C, Ravichandran KS. Living on the Edge: Efferocytosis at the Interface of Homeostasis and Pathology. Immunity. 2019; 50: 1149–1162. https://doi.org/10.1016/j.immuni.2019.04.018.

[5] Chen R, Zou J, Liu J, Kang R, Tang D. DAMPs in the immunogenicity of cell death. Molecular Cell. 2025; 85: 3874–3889. https://doi.org/10.1016/j.molcel.2025.09.007.

[6] Huy Nguyen ND, Fan CH, Huang SH, Liu W, Chen PT, Hsueh YY. Low-intensity pulsed ultrasound for peripheral nerve regeneration: mechanobiological mechanisms and translational potential. Journal of Translational Medicine. 2025; 24: 121. https://doi.org/10.1186/s12967-025-07638-1.

[7] Xuan M, Fan J, Khiêm VN, Zou M, Brenske KO, Mourran A, *et al*. Polymer Mechanochemistry in Microbubbles. Advanced Materials. 2023; 35: e2305130. https://doi.org/10.1002/adma.202305130.

[8] Zhang Y, Gao C, Li Y, Fu Q, Liu Y, Mo N, *et al*. Piezo-type mechanosensitive ion channel component 1: a mechano-bioenergetic transducer in the tumour microenvironment. Annals of Medicine. 2026; 58: 2603022. https://doi.org/10.1080/07853890.2025.2603022.

[9] Yu JL, Liao HY. Piezo-type mechanosensitive ion channel component 1 (Piezo1) in human cancer. Biomedicine & Pharmacotherapy = Biomédecine & Pharmacothérapie. 2021; 140: 111692. https://doi.org/10.1016/j.biopha.2021.111692.

[10] Song Y, Chen J, Zhang C, Xin L, Li Q, Liu Y, *et al*. Mechanosensitive channel Piezo1 induces cell apoptosis in pancreatic cancer by ultrasound with microbubbles. iScience. 2022; 25: 103733. https://doi.org/10.1016/j.isci.2022.103733.

[11] Tijore A, Margadant F, Dwivedi N, Morgan L, Yao M, Hariharan A, *et al*. Ultrasound-mediated mechanical forces activate selective tumor cell apoptosis. Bioengineering & Translational Medicine. 2024; 10: e10737. https://doi.org/10.1002/btm2.10737.

[12] Li Y, Fan Y, Zhao S, Cheng B. Ultrasound-triggered piezoelectric polyetheretherketone with boosted osteogenesis via regulating Akt/GSK3β/β-catenin pathway. Journal of Nanobiotechnology. 2024; 22: 539. https://doi.org/10.1186/s12951-024-02814-9.

[13] Nan K, Zhang L, Zhao Y, Yin S, Peng Y, Huang J, *et al*. The therapeutic potential of Piezo1 channel-mediated ferroptosis and its inhibitor. Apoptosis: An International Journal on Programmed Cell Death. 2026; 31: 107. https://doi.org/10.1007/s10495-026-02320-3.

[14] Wang S, Li W, Zhang P, Wang Z, Ma X, Liu C, *et al*. Mechanical overloading induces GPX4-regulated chondrocyte ferroptosis in osteoarthritis via Piezo1 channel facilitated calcium influx. Journal of Advanced Research. 2022; 41: 63–75. https://doi.org/10.1016/j.jare.2022.01.004.

[15] Tian D, Yang Z, Zhang J, Yang R, Hao H. The synergistic role of ferroptosis in osteosarcoma immunotherapy. Medical Oncology. 2025; 43: 61. https://doi.org/10.1007/s12032-025-03196-0.

[16] Mao Y, Du X, Wang W, Dong T, Zhu M, Niu J, *et al*. Melanin@PLGA/Nuciferine Nanoparticles for Enhanced Photothermal Therapy of Hepatocellular Carcinoma by Promoting Autophagy. International Journal of Nanomedicine. 2025; 20: 11081–11097. https://doi.org/10.2147/ijn.S536620.

[17] Liu Y, Cong K, Li Q, Zhang D, Sheng J. New insights into combined immunotherapy for hepatocellular carcinoma associated with liver cirrhosis. Frontiers in Immunology. 2025; 16: 1741398. https://doi.org/10.3389/fimmu.2025.1741398.

[18] Sheikh M, Khobragade D, Sakore A, Telrandhe U. Harnessing albumin's natural tumor-targeting properties: nanoplatform strategies for triple-negative breast cancer therapy. Discover Nano. 2026; 21: 3. https://doi.org/10.1186/s11671-025-04411-7.

[19] Barkóczi A, Képes Z, Szabó JP, Dienes RA, Károlyi PK, Papp T, *et al*. Metastasis and angiogenesis: preclinical PET study on hepatocellular carcinoma (He/De) tumor models. European Journal of Pharmaceutical Sciences: Official Journal of The European Federation for Pharmaceutical Sciences. 2025; 212: 107211. https://doi.org/10.1016/j.ejps.2025.107211.

[20] Liu Y, Li H, Hao YY, Huang LL, Li X, Zou J, *et al*. Tumor-Selective Nano-Dispatcher Enforced Cancer Immunotherapeutic Effects via Regulating Lactate Metabolism and Activating Toll-Like Receptors. Small. 2025; 21: e2406870. https://doi.org/10.1002/smll.202406870.

[21] Fang M, Zheng J, Song Q, Huang J, Cao R, Li P, *et al*. Breaking Apoptosis-Induced Immune Silence: Ultrasound-Activated Nano-Oncolytic Therapy Reinvigorates Antitumor Immunity. Advanced Materials. 2025; 37: e2508681. https://doi.org/10.1002/adma.202508681.

[22] Ma Z, Wang J, Zhang M, Liu W, Zhao L, Wang S, *et al*. Ultrasound Trigger Ultrasmall Multifunction Nanobubbles for Thrombus Visual Treatment. Advanced Healthcare Materials. 2025; 14: e2405075. https://doi.org/10.1002/adhm.202405075.

[23] Gongalsky MB, Tsurikova UA, Kudryavtsev AA, Pervushin NV, Sviridov AP, Kumeria T, *et al*. Amphiphilic Photoluminescent Porous Silicon Nanoparticles as Effective Agents for Ultrasound-Amplified Cancer Therapy. ACS Applied Materials & Interfaces. 2025; 17: 374–385. https://doi.org/10.1021/acsami.4c15725.

[24] Mitten EK, Baffy G. Mechanotransduction in the pathogenesis of non-alcoholic fatty liver disease. Journal of Hepatology. 2022; 77: 1642–1656. https://doi.org/10.1016/j.jhep.2022.08.028.

[25] Chen Y, Lin X, Qiu J, Sun Y, Wu B, Shang H, *et al*. Ultrasound-responsive nanobubble-mediated sonodynamic therapy sensitizes disulfidptosis in the treatment of liver hepatocellular carcinoma. Ultrasonics Sonochemistry. 2025; 118: 107368. https://doi.org/10.1016/j.ultsonch.2025.107368.

[26] Italiya KS, Mullins-Dansereau V, Geoffroy K, Gilchrist VH, Alain T, Bourgeois-Daigneault MC, *et al*. Ultrasound and Microbubble Mediated Delivery of Virus-Sensitizing Drugs Improves In Vitro Oncolytic Virotherapy Against Breast Cancer Cells. Ultrasound in Medicine & Biology. 2025; 51: 1124–1133. https://doi.org/10.1016/j.ultrasmedbio.2025.03.010.

[27] Karska J, Kowalski S, Saczko J, Moisescu MG, Kulbacka J. Mechanosensitive Ion Channels and Their Role in Cancer Cells. Membranes. 2023; 13: 167. https://doi.org/10.3390/membranes13020167.

[28] Shen X, Song Z, Xu E, Zhou J, Yan F. Sensitization of nerve cells to ultrasound stimulation through Piezo1-targeted microbubbles. Ultrasonics Sonochemistry. 2021; 73: 105494. https://doi.org/10.1016/j.ultsonch.2021.105494.

[29] Zheng B, Zhang H, Yu G, Geng R, Sang Y, Huang G, *et al*. Cascade Catalytic Nanozymes Induce Tumor Ca(2+) Overload and Ferroptosis by Reducing Energy Supply and Amplifying Oxidative Stress. ACS Applied Materials & Interfaces. 2025; 17: 33498–33512. https://doi.org/10.1021/acsami.5c04041.

[30] Xu Y, Ren M, Deng R, Meng J, Xu L, Zhao W, *et al*. UCNPs@PVP-Hemin-GOx@CaCO(3) Nanoplatform for Ferroptosis Self-Amplification Combined with Calcium Overload. Advanced Healthcare Materials. 2025; 14: e2404215. https://doi.org/10.1002/adhm.202404215.

[31] Xu W, Guan G, Yue R, Dong Z, Lei L, Kang H, *et al*. Chemical Design of Magnetic Nanomaterials for Imaging and Ferroptosis-Based Cancer Therapy. Chemical Reviews. 2025; 125: 1897–1961. https://doi.org/10.1021/acs.chemrev.4c00546.

[32] Pedrera L, Ros U, García-Sáez AJ. Calcium as a master regulator of ferroptosis and other types of regulated necrosis. Cell Calcium. 2023; 114: 102778. https://doi.org/10.1016/j.ceca.2023.102778.

[33] Wang S, Yi X, Wu Z, Guo S, Dai W, Wang H, *et al*. CAMKK2 Defines Ferroptosis Sensitivity of Melanoma Cells by Regulating AMPK–NRF2 Pathway. The Journal of Investigative Dermatology. 2022; 142: 189–200.e8. https://doi.org/10.1016/j.jid.2021.05.025.

[34] Li J, Jia YC, Ding YX, Bai J, Cao F, Li F. The crosstalk between ferroptosis and mitochondrial dynamic regulatory networks. International Journal of Biological Sciences. 2023; 19: 2756–2771. https://doi.org/10.7150/ijbs.83348.

[35] Liang FG, Zandkarimi F, Lee J, Axelrod JL, Pekson R, Yoon Y, *et al*. OPA1 promotes ferroptosis by augmenting mitochondrial ROS and suppressing an integrated stress response. Molecular Cell. 2024; 84: 3098–3114.e6. https://doi.org/10.1016/j.molcel.2024.07.020.

[36] Meier P, Legrand AJ, Adam D, Silke J. Immunogenic cell death in cancer: targeting necroptosis to induce antitumour immunity. Nature Reviews. Cancer. 2024; 24: 299–315. https://doi.org/10.1038/s41568-024-00674-x.

[37] Fang K, Yuan S, Zhang X, Zhang J, Sun SL, Li X. Regulation of immunogenic cell death and potential applications in cancer therapy. Frontiers in Immunology. 2025; 16: 1571212. https://doi.org/10.3389/fimmu.2025.1571212.

[38] Galluzzi L, Kepp O, Zitvogel L, Tang D, Kroemer G. Cancer cell death: Cell-autonomous and immunogenic dimensions. Cancer Cell. 2026; 44: 281–305. https://doi.org/10.1016/j.ccell.2025.12.005.

Editor's note: The Scientific Editors responsible for this paper were Xiaoyuan Ji and Kelong Fan.

Received: 6th March 2026; **Accepted**: 11th May 2026; **Published**: 29th May 2026